Dipl.-Ing. Stephanie Rošker, BSc

Zebra spectral structures in Jovian decametric radio emissions

MASTER'S THESIS

to achieve the university degree of

Diplom-Ingenieurin

Master's degree programme: Space Sciences and Earth from Space

submitted to

Graz University of Technology

Supervisor

Ao. Univ.-Prof. Mag. Dr. Helmut O. Rucker

Department of Physics, University of Graz

Dr. Mykhaylo Panchenko
Space Research Institute Graz, Austrian Academy of Sciences

Graz, February 2016

AFFIDAVIT

I declare that I have authored this thesis independently, that I have not used other than the declared sources/resources, and that I have explicitly indicated all material which has been quoted either literally or by content from the sources used. The text document uploaded to TUGRAZonline is identical to the present master‘s thesis dissertation.

Date

Signature

Abstract

Jupiter emits intense coherent non-thermal radio waves in a wide frequency range. The strongest component of the Jovian radio emissions is the decametric emission (DAM) with wavelengths in the range of tens of meters and frequencies from a few megahertz up to 40 MHz. Zebra stripe-like spectral structures in the Jovian DAM emissions have been registered for the first time during two observation campaigns from September 2012 to March 2014 by the URAN-2 telescope in Poltava, Ukraine.

The aim of this thesis is to characterize the patterns and analyse them statistically. The investigations reveal that the zebra structures are a non-Io related phenomenon. One central result is the possibility to localize the zebra structures in respect of Jupiter; the sense of polarization of the zebra emissions defines the hemisphere of origin. The structures can now be clearly identified, as their frequency properties have been recorded. The driving force of the phenomenon turns out to be the magnetic field, which is in accordance with other planetary radio effects. On the basis of these results the generation mechanism is studied. Therefore, the Double Plasma Resonance theory for electrons, which is widely accepted for explaining similar structures at the Sun and in lower Jovian frequency ranges, is applied. Estimations of the closest possible generation sites are obtained. However, when calculating the electron density, an essential plasma parameter, the theory provides values that cannot be realized in the vicinity of Jupiter. Proposals for future proceedings are given that will initiate further investigations. The thesis also contains a chapter on the concepts and basic principles employed throughout the study.

Kurzfassung

Jupiter emittiert intensive, kohärente, nicht-thermische Radiowellen in einem breiten Frequenzbereich. Die stärkste Komponente der Jupiter-Radioemissionen ist die Dekameter-Emission (DAM) mit Wellenlängen im Bereich von mehreren zehn Metern und Frequenzen von einigen Megahertz bis zu 40 MHz. Zebrastreifenartige Spektralstrukturen in Jupiter-DAM wurden erstmals während zweier Beobachtungskampagnen von September 2012 bis März 2014 vom URAN-2 Teleskop in Poltava, Ukraine, erfasst.

Das Ziel dieser Masterarbeit ist die Charakterisierung und statistische Analyse dieser Strukturen. Die Untersuchungen zeigen, dass die Zebra-Strukturen ein von Io unabhängiges Phänomen sind. Ein zentrales Ergebnis ist die Möglichkeit der Lokalisierung der Zebra-Strukturen in Bezug auf Jupiter; die Polarisationsrichtung der Zebra-Emissionen definiert die Halbkugel der Entstehung. Die Strukturen können nun eindeutig identifiziert werden, da ihre Frequenzeigenschaften protokolliert sind. Als treibende Kraft des Phänomens erweist sich das Magnetfeld; dies stimmt mit anderen planetaren Radioeffekten überein. Auf Basis dieser Resultate wird der Erzeugungsmechanismus untersucht. Dafür wird die Double Plasma Resonance Theorie für Elektronen, die für die Erklärung ähnlicher Strukturen bei der Sonne und in niedrigeren Frequenzbereichen von Jupiter weitgehend akzeptiert ist, herangezogen. Abschätzungen für die nächstgelegensten Erzeugungsorte werden erhalten. Bei der Berechnung der Elektronendichte, einem wesentlichen Plasmaparameter, liefert die Theorie allerdings Werte, die in der Umgebung von Jupiter nicht realisiert werden können. Anregungen für zukünftige Vorgehensweisen werden gegeben, die weitere Untersuchungen anstoßen werden. Die Masterarbeit enthält des Weiteren ein Kapitel über die Konzepte und Grundbegriffe, die in dieser Studie zur Anwendung kommen.

Acknowledgements

I would like to thank the Commission for Astronomy of the Austrian Academy of Sciences for the financial support by the Oelzelt-Newin foundation and the Space Research Institute in Graz for providing the infrastructure.

I want to express my gratitude to Prof. Helmut O. Rucker for his supervision. I also thank Dr. Mykhaylo Panchenko for his guidance.

Contents

1 Introduction

In our solar system Earth, Jupiter, Saturn, Uranus and Neptune emit radiation in the radio frequency range. These emissions play an integral role in remote sensing and are driven by the interaction of the planetary magnetic field and mainly external electrically charged particles entering the magnetosphere. The aurora regions of the above mentioned planets are a source of very intense low frequency radio waves.

Jupiter is of special interest as it offers a wide spectral range of radio emissions due to its strong magnetic field. The vast magnetosphere, which is also the largest planetary magnetosphere in the solar system, guarantees high intensity signals. Jupiter is known to emit intense coherent non-thermal radio waves in a wide frequency range. The strongest component of the Jovian radio emissions is the decametric emission (DAM) with wavelengths in the range of tens of metres and frequencies from a few megahertz up to 40 MHz. Jovian radio emissions are partly influenced by the Galilean moon Io, which has its own ionosphere and thus acts as an internal plasma source in the Jovian magnetosphere. Certain longitudes on Jupiter in combination with certain positions of Io in respect to Jupiter favour radio emissions. Therefore, Jupiter emission can be divided into Io-dependant and non-Io-dependant emissions.

The DAM emissions were the first to be detected on Earth (by Burke and Franklin [1] in 1955 well before the terrestrial radio emissions!) as the DAM waves are the sole radio signals to travel through the Earth's ionosphere and can so be observed by ground-based instruments. The advantage of ground-based instrumentation is its ability of handling large data transmission rates and storage capacities. These requirements are needed to provide the high time and frequency resolutions of the observations. [2, 3, 4, 5, 6, 7]

Observations at the URAN-2 telescope in Poltava, Ukraine, between September 2012 and March 2014 showed zebra stripe-like patterns at high frequencies of DAM. These structures have never been reported before in this frequency range although similar stripes have been observed in lower Jovian frequency ranges (kilometric radiation, KOM) and at the Sun. The logical consequence is to investigate whether those structures resemble any already known phenomenon. The results of the characterisation and the statistical analysis of the zebra structures, that are performed in this thesis, should eventually provide the basis for the theoretical framework of the Jovian DAM zebra patterns and initiate further investigations.

The present thesis covers the following topics: Chapter 2 comprises a collection of beneficial background information. The lexically structured chapter consists of several self-contained sections on keywords the reader might come across when delving into the chapters on the evaluation of Jovian zebra patterns. Chapter 3 describes the data acquisition process and introduces the dynamic spectra that have been analysed. Chapter 4 provides the detailed statistical investigations of the zebra stripes. In chapter 5 the influence of the magnetic field and the generation mechanism are discussed. The Double Plasma Resonance (DPR) theory is tested on the Jovian DAM zebra structures. Chapter 6 presents the conclusion; chapter 7 gives an outlook on potential future proceedings. Chapter 8 finally summarizes the matter.

2 Fundamentals

This chapter forms a glossary of the concepts and basic principles applied throughout the investigations of the Jovian DAM zebra spectral structures. It can be seen as a reference work and consulted when further information on a certain topic dealt with in the rear chapters is required. The sections are arranged alphabetically and are self-contained. There is no strict connection between the single articles, therefore they can be read individually. Additional material on all topics covered can be found in cited literature.

2.1 Central Meridian Longitude (CML)

To localize the zebra structures on Jupiter, the central meridian longitude is used. The central meridian represents a fixed longitude line on Jupiter that rotates with Jupiter's interior as defined by the System III period. The CML measures the angle that the central meridian draws in direction to Earth. [8]

2.2 Cyclotron Maser Instability (CMI)

The cyclotron maser instability theory is regarded to be the dominant mechanism of the planetary auroral non-thermal radio emission. Electrons approaching a radio planet enter into regions of converging magnetic field lines and are mirrored magnetically at certain altitudes. On their return path the particle population has changed, as some electrons got lost due to particle collisions in the ionosphere. This variation in the particle population is responsible for the generation of planetary radio emission. Every particle distribution that deviates from uniform distribution tends to restore equilibrium. In the compensation process energy is released that supplies the generation mechanism of non-thermal radio emission.

The cyclotron maser instability is an interaction based on resonance between particle and wave. An electron that gyrates around a magnetic field line emits an electric field due to the acceleration it experiences during this cyclotron motion. If the electric field vector gyrates in the same direction as the electron and is at constant phase with the motion of the electron for a longer time, the wave is at resonance with the electron. The CMI theory includes the relativistic effect in the cyclotron resonance condition [9]. Several substantial properties of radio emissions result from the CMI theory. On the one hand, the emitted radio frequency is close to the local gyrofrequency. This means that the altitude of the generation site can be derived from the emission frequency or the magnetic flux density respectively. A similar calculation is performed in section 5.2.1 for the zebra structures, however by applying the Double Plasma Resonance (DPR) theory. On the other hand, the CMI theory favours the generation of extraordinary electromagnetic waves (X mode; waves that are influenced by the magnetic field) compared to the ordinary mode (O mode) that is unaffected by the magnetic field. The theory predicts the highest amplification for the right-hand (RH) polarized extraordinary mode (RX mode, by definition the electron - and the electric field - gyrates clockwise when the line of sight is the same direction as the magnetic field vector is pointing to). The radio wave emission occurs almost perpendicular to the magnetic field direction and is beamed into a thin-walled, hollow cone (see section 2.7, in particular Figure 4). [10]

2.3 Double Plasma Resonance (DPR)

First theories on the generation mechanism of solar zebra appeared in the early 1970s. The Double Plasma Resonance model [11] evolved into a widely accepted theory capable of describing the phenomenon. First, zebra patterns were thought to be connected to the excitation of harmonically-related plasma waves (e.g. Bernstein modes) but such models cannot explain the generation of non-equidistant stripes. This property has been found for both solar and Jovian low frequency zebra structures. For these phenomena the production of each zebra stripe at different locations is more adequate (see Figure 1).

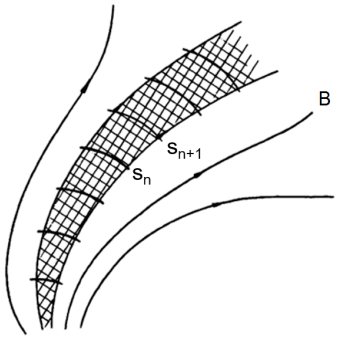

Figure 1: Generation of zebra stripes at different locations. In the source region around one field line each zebra stripe is produced individually at the harmonic level s. Higher harmonic numbers s correspond to lower emission frequencies. [11]

Kuznetsov and Vlasov [12] elucidate the model like this: in the DPR model it is assumed that an electron beam with unstable distribution (e.g. loss cone type) excites upper-hybrid plasma waves which are subsequently transformed into electromagnetic waves due to non-linear processes. The generation efficiency of the plasma waves is higher if their frequency, which is close to the upper hybrid frequency f_{uh}, coincides with a harmonic s of the electron cyclotron frequency f_{ce}

$$f_{uh} = \sqrt{f_{pe}^2 + f_{ce}^2} \approx s\ f_{ce}$$

with f_{pe}, the plasma frequency for electrons and $s = 2, 3, 4, ...$ Under the condition of $f_{pe} > f_{ce}$ the plasma resonance is only possible for $s \geq 2$. It is emphasized that the frequency spacing between adjacent stripes can be variable and defined only by the magnetic field and plasma density profiles, therefore the harmonic number s does not necessarily have to be an integer. Kuznetsov and Vlasov were able to reproduce observed zebra patterns with the DPR model.

Zebra structures at the Sun and in different Jovian frequency regions occur rarely. That means that the required conditions (unstable electron distribution and fulfilling the resonance condition) are only met seldom [12]. Nevertheless, the zebra structures can serve as remote sensing tool of the Jovian magnetosphere if the location of the generation site can be determined. The data available for this study can provide this information and targets at linking the properties derived by the statistical analysis of the Jovian zebra patterns to the generation mechanism. This could be one step into the direction of retrieving additional knowledge from the observed Jovian DAM zebra phenomenon.

2.4 Dynamic spectra

Radio-astronomical observations are usually depicted in dynamic spectra. Intensity is displayed as a function of time and frequency. Darkening or colour represents intensity, the x-axis represents time, the y-axis the frequency. [13, 2] Several examples are displayed in chapter 3. In grey-scale images white stands for minimum intensity, black for maximum intensity, in colour images blue represents the minimum and red the maximum intensity.

The URAN-2 radio telescope also records the polarization of the radiation. Polarization is displayed in dynamic spectra as well. Again time and frequency are represented on the x- and y-axis, however, the shading or colour stands for the polarization (RH polarized = black/blue , left-hand (LH) polarized = white/red). See section 2.12 for details on the polarization measurement.

2.5 Faraday effect

The Faraday effect is a magneto-optical phenomenon acting on polarized radiation and induces the rotation of the plane of polarization of the radiation. The rotation is linearly proportional to the magnetic field component in direction of propagation. LH and RH circularly polarized waves experience a slightly different refraction index in a magnetic field, thus the differently polarized waves travel at slightly different speeds. This causes the shift in polarization since a polarized wave can either be decomposed into two linearly polarized waves (orthogonal directions) or two circularly polarized waves (opposite direction of polarization). [14, 15, 16]

The rotation angle ψ is proportional to the wavelength λ and the rotation measure RM:

$$\psi = \lambda^2 \text{ RM}$$

with

$$\text{RM} \propto \int_L n_e(l)\ B(l)\ dl$$

when the magnetic field B and/or the electron density n_e is not constant along the path l. [17]

In the case of wave propagation from Jupiter to Earth Faraday rotation is produced in different regions [18]:

- 10 - 30 % in Jupiter's magnetosphere and the Io plasma torus
- a few % in the interplanetary medium
- 70 - 90 % in the terrestrial ionosphere

The polarized wave travels through several magneto-plasmas of different densities on its way from Jupiter to Earth. Certain frequencies can be received optimally by a linearly polarized antenna due to the optimal orientation of the electric field vector which is rotated due to the effect described above. This ideal reception appears as intensity maximum in the spectrum. For other frequencies the reception results in lower intensity. These Faraday fringes represent the variation of the electron content along the radiation path. In the Jovian dynamic spectra the effect appears as parallel horizontal fringes with increasing

spacings with increasing frequency of appearance due to its λ^2 dependence (see Figure 2) and should not be confused with zebra structures. Specifically at URAN-2 the influence of the Faraday effect comes into effect because the linearly polarized antennas receive highly elliptically polarized emission.

In addition, the Faraday effect can be used as a remote sensing tool for analysing distant magneto-plasmas. [10]

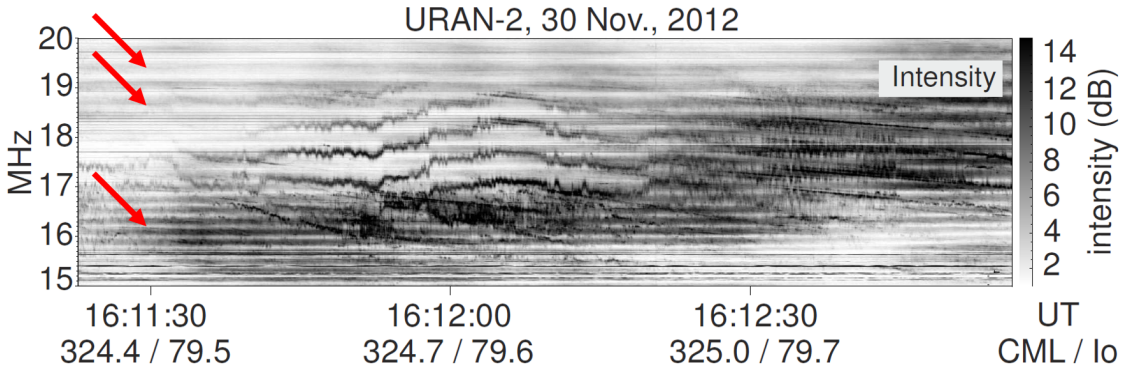

Figure 2: Faraday effect in a dynamic spectrum of Jupiter. Red arrows point to the fringes caused by the Faraday effect. The frequency dependence can be clearly seen. [19]

2.6 Influences on DAM

The Jovian decametric radio emission (DAM) with frequencies from a few to 40 MHz (corresponding to wavelengths of 100 m to approx. 10 m wavelength) is the only planetary radio emission apart from Saturn electric discharges (SED) that can be observed from the ground [20] due to the limited opacity of the Earth's atmosphere for long-wavelength radio waves (see Figure 3).

This study is only interested in zebra spectral structures that occur in this DAM frequency range. Nevertheless several undesirable effects can be found in the spectra, such as influences due to the Faraday effect (see section 2.5) and ionospheric scintillation (see section 2.8).

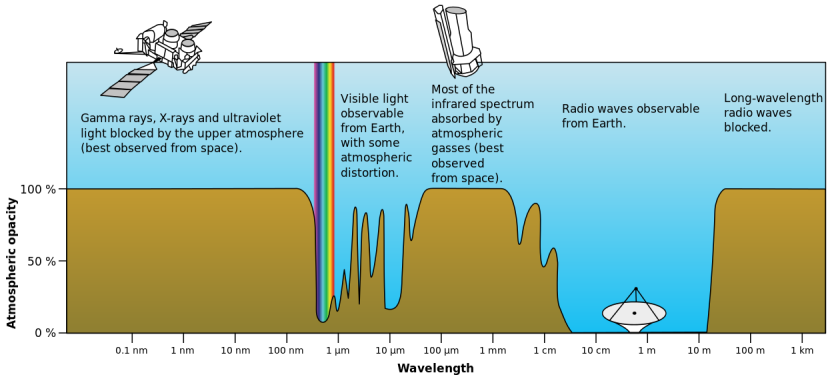

Figure 3: Atmospheric electromagnetic opacity [21]. The large window in the radio frequency range enables ground-based radio astronomy.

2.7 Io and its decametre radio emission

Most of the inner-magnetospheric thermal plasma of Jupiter originates from its moon Io. Io experiences changes in its orbit due to gravitational forces from other Galilean moons (Europa, Ganymede). This in turn leads to changes of the tidal forces of Jupiter, so that Io is constantly exposed to energy dissipation in its interior. The resulting heating can be observed via the active volcanoes on Io. The so-called Io torus forms around the Io orbit (distance from Jupiter = 5.91 Jovian radii R_J) and co-rotates almost rigidly with Jupiter. However, the plasma torus consisting of sulphur and oxygen atoms is controlled by the magnetic field.

Due to the complex interaction of Io with the surrounding magnetospheric plasma a current system is induced along the Io flux tube which triggers the emission of intensive non-thermal radio radiation in the vicinity of Jupiter. Io has an orbital period of 42.46 h around Jupiter and is situated in a constant flow of co-rotating magnetospheric plasma (rotates with 9.93 h). In this plasma flow an electric field is generated. The electric potential difference across the diameter of Io (perpendicular to the flux tube) induces a current deriving from Io into the northern and southern Jovian hemispheres. This current is directed towards Jupiter along the outer field lines (more distant to Jupiter) of the flux tube and back to Io along the field lines closer to Jupiter (see Figure 4).

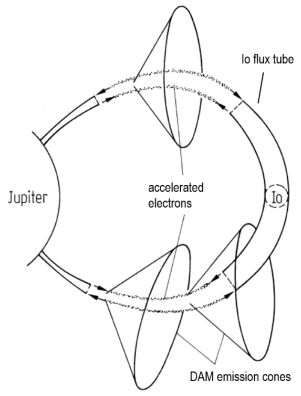

Figure 4: Schematics of the Io triggered decametre radio emission (DAM), its emission in cones and the Io flux tube. If a radio beam inside one of the envelopes of a cone points towards Earth the emission can be received by ground-based telescopes due to the high frequency that can penetrate the terrestrial ionosphere. [10] The Io flux tube is defined by the field lines that clamp Io.

The electric circuit is closed by currents perpendicular to the field lines in the Jovian ionosphere and in the ionosphere of Io respectively. The electrons that are accelerated along the converging magnetic field lines towards Jupiter can generate electromagnetic radiation (according to Cyclotron Maser Instability (CMI) theory, see section 2.2). Due to the high magnetic flux density close to Jupiter the frequency of this radio emission is high. The Io emission features frequencies in the MHz-range with a maximum frequency of 39.5 MHz (defined by the magnetic field with the rule of thumb $f_{ce} \cong 2.8\ B$ with $[B]$ = G and $B_{max} \approx 14$ G $\rightarrow f_{max} = 39.5$ MHz). This corresponds to wavelengths in the decametre range (DAM) which can penetrate the Earth's ionosphere and thus be registered by ground-based radio telescopes. Io's influence was detected in 1964 [22], several years after the discovery of Jupiter's radio emission in 1955 [1]. Decades of observations

uncover a clear pattern: when Jupiter is connected to Io within a certain range of longitude (i.e. within certain magnetic field regions) via the Io flux tube, radio emission is produced with a certain probability. Io's position in respect to the observer is essential for the observation of the DAM emission because the radio beam (corresponds to a part of the envelope of the emission cone) has to hit the observer. The occurrence of DAM as functions of Jupiter longitude (Central Meridian Longitude, CML) and Io phase is displayed by gradual black shading in Figure 5. Several Io-radio-sources appear in the diagram: Io-A, Io-B, Io-C and Io-D. However, there exist CML regions (e.g. $230° \leq \text{CML} \leq 280°$, so-called non-Io-A) where the decametre emission is independent of Io's position. They are called non-Io sources.

Radio emissions influenced by Io occur in various ranges of time: radio storms last over several hours and feature internal arc structures that change within minutes. Scintillation effects are fluctuations of intensity due to plasma density variations that occur within seconds. S-bursts (S for short) emerge in the millisecond regime and are also known as milliseconds-radio-bursts.

The Io decametre radio emission is not the sole Jupiter radio emission. Jupiter emits radio signals in a very broad frequency range. Ground-based instrumentation can only register Jupiter emission in the MHz-range, whereas space probes, such as Voyager, Ulysses or Cassini investigated the kHz-range. [10]

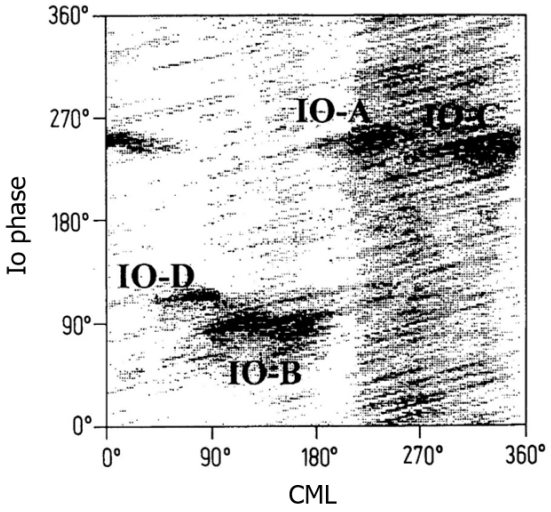

Figure 5: Occurrence of Jovian DAM as functions of CML and Io phase indicated by black shading (from [23]). The Io-A, Io-B, Io-C and Io-D sources are labelled.

2.8 Ionospheric scintillation

The terrestrial ionosphere ranges from approximately 60 up to 1000 km above the Earth's surface and contains large amounts of free charge carriers. Radio waves travelling across the ionosphere are reflected, absorbed, refracted and scattered causing a loss of energy. Ionospheric scintillation describes the fluctuation of the radio signals that is induced by the interaction with irregular structures of various scales in the ionosphere. [24] These irregularities vary with time of day, season, latitude, solar and magnetic activity and

frequency. They predominantly occur in the F layer at altitudes from 200 to 1000 km. The equatorial regions ± 20° in latitude around the magnetic equator and high latitude regions are particularly affected. Globally, a maximum during night-time can be observed. At the equator activity begins directly after sunset. In polar regions more scintillation occurs during the dark months. [25]

2.9 Io phase

Jupiter's radio emissions are partly influenced by its moon Io, which has its own ionosphere and acts as an internal plasma source in the Jovian magnetosphere. These influences depend on the position of Io in respect to Jupiter as seen from an observer. Io's position is determined by the Io phase. Figure 6 depicts the definition of the Io phase. Io is at 0° when it is located directly behind Jupiter as seen from an observer. It increases with the direction of Io's orbit. [10]

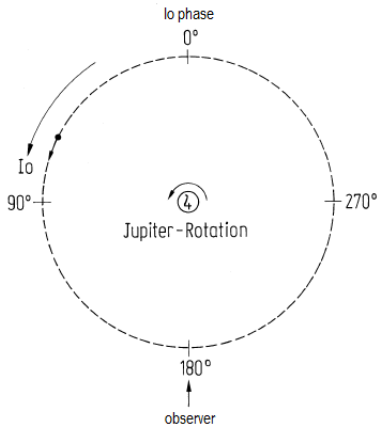

Figure 6: Io phase definition [10]

2.10 Jovian magnetic field

Jupiter features the strongest planetary magnetic field in the solar system. The source for all planetary magnetic fields is the motion in the electrically conducting interior which generates electrical currents and associated magnetic fields by the dynamo process. In case of Jupiter this motion takes place in a metallic hydrogen core (iron core for Earth). [26] The strong internal field together with the magnetic fields coming from the currents in the magnetopause withstands the kinetic pressure of the solar wind. Compared to the Earth's orbit the plasma density of the solar wind in the Jovian orbit (approx. 5 AU distance from the Sun) is only 1/25. The interaction of the magnetic field and the solar wind results in a huge magnetosphere, which extends up to $7 \cdot 10^6$ km (50 to 100 Jovian radii R_J) on the day-side while the magnetotail on the night-side stretches out to the orbit of Saturn. Thus, the Jovian magnetosphere is the largest structure in the solar system apart from the solar wind. Figure 7 illustrates the Jovian magnetosphere with the 4 Galilean moons. In

contrast to the terrestrial magnetosphere, which is fuelled by the solar wind, the dominant source of plasma for Jupiter is its satellite Io with its active volcanoes. [10, 27]

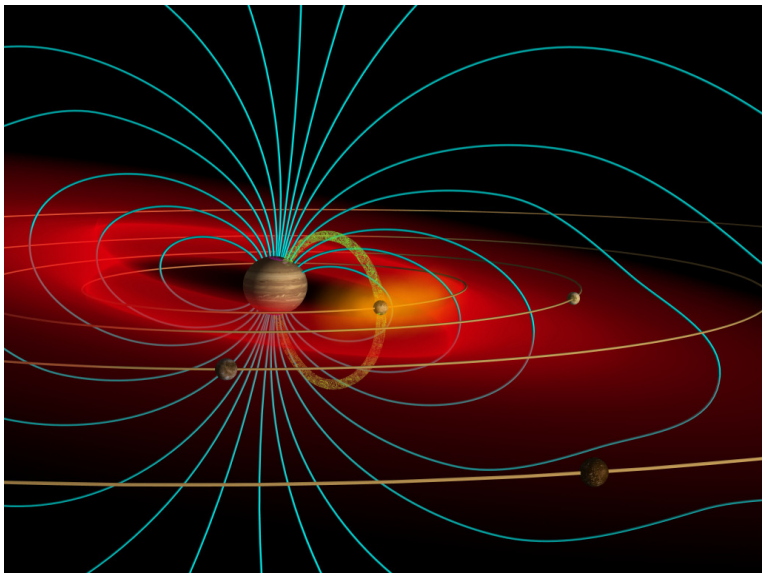

Figure 7: Jovian magnetosphere with the 4 Galilean moons Io (distance from Jupiter: 5.9 R_J), Europa (9.5 R_J), Ganymede (15.0 R_J) and Callisto (26.5 R_J) and their orbits (yellow). The light green tube between the innermost moon Io and Jupiter represents the Io flux tube. Several magnetic field lines are drawn in blue. [28]

The Jovian field has been remotely studied by radio astronomers since 1957, well before spacecraft in-situ observations. The magnetic field was discovered by analysing ground based observations of non-thermal radio emissions with regard to frequency and polarization properties of the signals. Thereby, the global field configuration could be derived quite well. This knowledge was expanded by subsequent in-situ spacecraft observations. Pioneer 10, the first space probe measuring the Jovian magnetic field, confirmed the ground-based estimations in 1973. [26]

The first model of the Jovian magnetic field (Goddard Space Flight Center O4 Model - GSFC O4, up to order 3) was developed in 1974 by Acuña and Ness [29] and showed that the field significantly deviates from the dipole structure known from the terrestrial field. The field exhibits large quadrupole and octupole terms, which induce the field to be very complex lacking polar symmetry. In the northern hemisphere the field features values of up to approx. $14 \cdot 10^{-4}$ T = 14 G, in the South the maximum values lie around $10.5 \cdot 10^{-4}$ T = 10.5 G which correspond to about 20 times the terrestrial values.

By assuming the region of space in close proximity to a planet to be free of electrical currents the magnetic flux density B can be derived from the scalar potential ϕ:

$$B = -\nabla\phi$$

The scalar potential ϕ can be decomposed into a set of orthogonal functions, the spherical harmonics [30]:

$$\phi(r) = R_J \sum_{n=1}^{\infty} \left(\frac{R_J}{r}\right)^{n+1} \sum_{m=0}^{n} \{P_n^m(\cos\theta)\,[g_n^m \cos(m\varphi) + h_n^m \sin(m\varphi)]\}$$

where R_J is the radius of Jupiter, r is the radial distance to the planet's centre and the angles θ and φ are latitude and longitude, respectively. The $P_n^m(\cos\theta)$ are Schmidt-normalized associated Legendre functions of degree n and order m, and g_n^m and h_n^m represent the spherical harmonic coefficients (Schmidt coefficients). The determination of the coefficients g_n^m and h_n^m is the principal task for planetary magneticians. [26]

Table 1: Schmidt normalized spherical coefficients for the VIP4 model. The coefficients are in Gauss, referenced to Jupiter system III (1965) coordinates, and R_J = 71323 km. UR refers to unresolved parameters. [31]

coefficient	VIP4	coefficient	VIP4	coefficient	VIP4
g_1^0	4.205	g_3^0	-.016	g_4^1	0.222 (.48)
g_1^1	-.659	g_3^1	-.520	g_4^2	-.061 (.89)
h_1^1	0.250	g_3^2	0.244	g_4^3	-.202 (.94)
g_2^0	-.051	g_3^3	-.176	g_4^4	0.066 (UR)
g_2^1	-.619	h_3^1	-.088	h_4^1	0.076 (UR)
g_2^2	0.497	h_3^2	0.408	h_4^2	0.404 (.93)
h_2^1	-.361	h_3^3	-.316	h_4^3	-.166 (.89)
h_2^2	0.053	g_4^0	-.168 (.75)	h_4^4	0.039 (UR)

It turned out that a spherical harmonic expansion to degree and order 3 or 4 was sufficient to represent the internally generated magnetic field. The long-time standard GSFC O4 model was eventually improved by further observations and considerations into the VIP4 model (Voyager, Io footprint, Pioneer). It uses observations from the Pioneer and Voyager missions up to degree 4 and order 4 and takes the Io footprint into consideration. [31] See Table 1 for the Schmidt coefficients of the VIP4 model. The Io footprint depicts a constraint to the magnetic field configuration. Emissions have been observed that follow a path around the Jovian magnetic poles and coincide with Io's orbital motion. The emission sites match the footprints of the field lines that are attached to Io at a distance of 5.9 R_J. This docking of the Io flux tube thus defines the region where field lines with an equatorial distance of 5.9 R_J must pass. See Figure 4 for an illustration of the Io flux tube. In order to consider this restriction the surface magnetic field, which is particularly prone to imprecision, as no in-situ observations are available and the higher degree and order terms dominate, had to be represented more accurately than previous models - the VIP4 model was developed [31].

The VIP4 model is used as basis for the Jovian magnetic field configuration in this thesis. It sufficiently maps the magnetic field structure for the purposes in this study, even though further developments have been achieved (VIPAL model [32]). These improvements mainly focus on a better description of auroral processes which require exact modelling of the polar regions.

Figure 8 displays contour plots of the magnetic flux density on the surface and in a distance of 1 R_J above Jupiter according to the VIP4 model with a scale in Gauss. The x-axis represents the longitude on Jupiter, the y-axis stands for the latitude. The magnetic flux density is colour-coded with red for the maximum and blue for the minimum value. It becomes clear, that the magnitude of the higher multipole moments (quadrupole: n = 2, octupole: n = 3, ...) decreases faster with increasing distance than the dipole terms. In larger distances the dipole character of the magnetic field structure dominates. [10] This

fact justifies the dipole approach of the magnetic field structure in section 5.2.

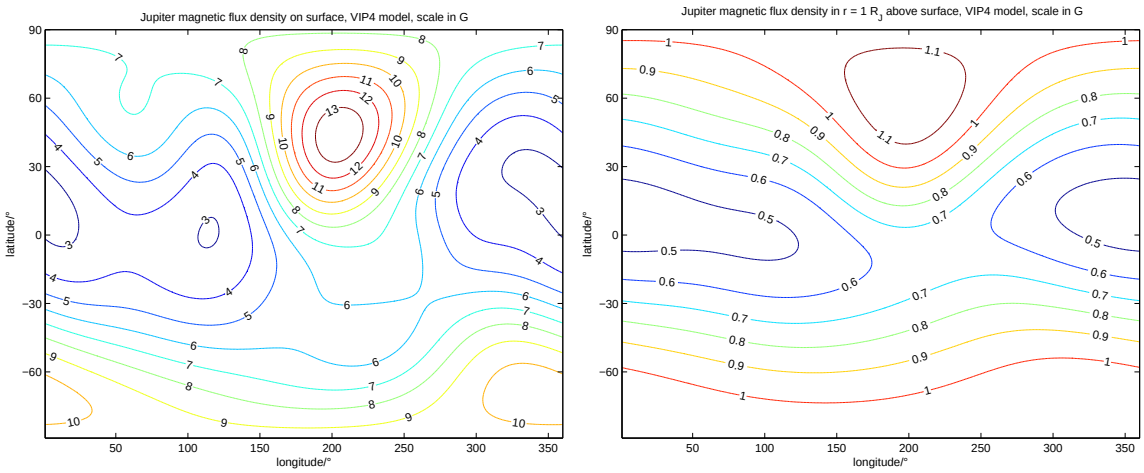

Figure 8: Magnetic flux density on the surface (left) and in 1 R_J distance above Jupiter (right) according to the VIP4-model. The x-axis represents the longitude on Jupiter, the y-axis stands for the latitude. The magnetic flux density is colour-coded with red for the maximum and blue for the minimum value. The scale is in G.

2.11 Magnetic field description

The magnetic field can be described by the magnetic field strength $\vec{H}$ and the magnetic flux density $\vec{B}$ with the units $[\vec{H}] = \frac{\mathrm{A}}{\mathrm{m}}$ and $[\vec{B}] = \frac{\mathrm{kg}}{\mathrm{As}^2} = \frac{\mathrm{N}}{\mathrm{mA}} = \mathrm{T} = 10^4$ G. In vacuum those physical values are connected by the physical constant μ_0 ($[\mu_0] = \frac{\mathrm{kgm}}{\mathrm{A}^2\mathrm{s}^2} = \frac{\mathrm{N}}{\mathrm{A}^2}$):

$$\vec{B} = \mu_0 \vec{H}$$

Alternatives names for $\vec{B}$, $\vec{H}$ and μ_0 are listed in Table 2. Throughout this thesis the absolute value of the magnetic flux density B measured in Gauss ($1\ \mathrm{G} = 10^{-4}\ \mathrm{T}$) is used to express the magnetic field.

Table 2: Alternative names for $\vec{B}$, $\vec{H}$ and μ_0 [33]

$\vec{B}$	$\vec{H}$	μ_0
magnetic flux density magnetic induction magnetic field	magnetic field strength magnetic field intensity magnetic field magnetizing field	vacuum permeability permeability of free space permeability of vacuum magnetic constant

2.12 Polarization

Electromagnetic waves are transversal waves where the magnetic and electric field vector are always perpendicular to the direction of propagation and can thus exhibit polarization. By convention the direction of the electric field defines the polarization. When the electric

field vector oscillates in only one plane, the wave is linearly polarized. If the vector describes an ellipse along the direction of propagation the wave is elliptically polarized. Circularly polarized waves are a special case of elliptical polarization. Here the electric field vector draws a circle around the propagation vector. These circumstances are illustrated in Figure 9. The direction of rotation of the electric field defines the sense of polarization for circularly or elliptically polarized waves, either RH or LH polarized. [34]

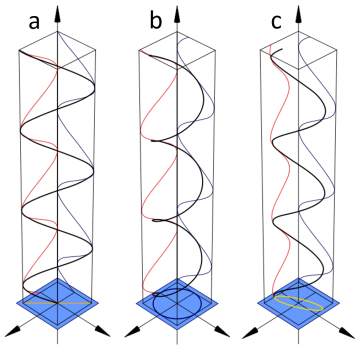

Figure 9: Composition of linearly (a), circularly (b) and elliptically (c) polarized waves of linearly polarized components. The electric field vector is displayed in black, the linearly polarized components in red and blue. The electric field vector is projected onto the blue plane and visualizes the polarization. [35]

For the sense of polarization (RH or LH) there exist two contrary definitions. For radio astronomy the convention by the International Astronomical Union (IAU) resolution made in 1973 [36] is in use, which is also used in the engineering community (standard by the Institute of Electrical and Electronics Engineers (IEEE) 149-1979 (R2008) [37]) and in quantum physics, as stated by Richard Feynman in his lectures [38]:

> If the end of the electric vector, when we look at it as the light comes straight toward us, goes around in a counterclockwise direction, we call it right-hand circular polarization. [...] Our convention for labelling left-hand and right-hand circular polarization is consistent with that which is used today for all the other particles in physics which exhibit polarization (e.g., electrons). However, in some books on optics the opposite conventions are used, so one must be careful.

This definition is valid in this thesis and is vital to explain an observational effect that characterizes the zebra structures (section 4.2). By assuming the zebra signals to be emitted in RX-mode as has been observed for planetary radio phenomena (see section 2.2), it is possible to determine the source region of the zebra emission as the sense of polarization of the observed radiation can be assigned to either the northern or southern Jovian hemisphere. Jupiter's magnetic field points in the opposite direction compared to the terrestrial field [39], the magnetic north pole is situated on the northern hemisphere. Thus, the field lines point from Jupiter's north to its south pole (by definition magnetic field lines point from the northern to the southern pole). Imagine a zebra event that is generated in the northern hemisphere. A wave emitted in RX-mode leaves Jupiter along the field line and reaches an observer as RH polarized wave because electrons gyrate counter-clockwise along the magnetic field when the wave is approaching an observer. If the event is generated in

the southern hemisphere the emission is again in RX-mode but the field line now points in the opposite direction. Therefore the electrons gyrate around the field lines in clockwise direction for an observer and appear as LH polarized radiation. RH polarized radiation can be allocated to the northern hemisphere of Jupiter and LH polarized radiation to the southern Jovian hemisphere. This effect is illustrated in Figure 10.

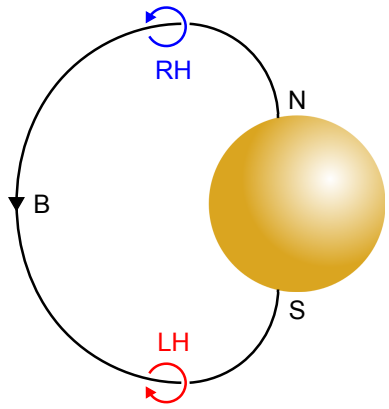

Figure 10: Illustration of emission of waves in RX mode from different hemispheres. Jupiter with one exemplary magnetic field line is shown. The direction of the magnetic field is indicated by the arrow on the field line pointing from north (N) to south (S). The blue arrow shows a wave emitted in RX mode from the northern hemisphere that is observed as RH polarized wave. The red arrow depicts a wave emitted in RX mode in the southern hemisphere which appears as LH polarized wave when observed.

Analysing the polarization of planetary radio emission is vital as it can affect the emission process and the wave propagation in the plasma surrounding the source. All planetary auroral emissions are strongly polarized. [20] The kilometric and hectometric emissions of Earth, Jupiter, Saturn, Uranus and Neptune were observed as purely circular. Only for some pulsars and Jupiter's decametre emission (DAM) the rare elliptical polarization could be recorded. Again, this is just an observational effect. Elliptical polarisation is not directly generated but develops during wave propagation. One condition that could explain the existence of elliptical polarization for Jovian DAM claims the very low plasma density in the low altitude polar magnetosphere of Jupiter. [40]

Also the zebra spectral structures, which appear in decametre frequency ranges, are highly polarized, they feature elliptical polarization. At the URAN-2 telescope where the zebra structures have been observed, polarization spectra have been recorded additionally to the intensity dynamic spectra. In these polarization spectra (see Figure 18c) the normalized Stokes parameter of circular polarization V is recorded. According to the standard IRE 1942 defined by the Institute of Radio Engineers [41] negative values of V correspond to RH polarization and positive values to LH polarized emissions. The Stokes parameters I, Q, U, V describe intensity (I) and polarization of a wave (Q and U for linear polarization and V for circular polarization [42]). URAN-2 can measure all Stokes parameters which corresponds to measuring the full state of polarization. However, the sophisticated calibration process for the large antenna array still has to be performed. So far only the parameter V can be determined for qualitative statements. The sense of polarization is provided but not the exact degree of total polarization. [19]

2.13 Radio astronomy

Radio astronomy describes the techniques to receive and measure radio waves and has been developed since the 1930s when Karl Jansky (the non-SI unit for the spectral flux density is named after him: 1 Jy = 10^{-26} $\frac{\mathrm{W}}{\mathrm{m^2 Hz}}$) detected lightning radio emission and the emission from the Galactic centre. In contrast to optical or high-energy astronomy where intensity is detected, the amplitude and phase of the electric field of the incoming waves is recorded in radio astronomy. This facilitates interferometry which can compensate for the low angular resolution ($\propto \lambda/D$ with D the diameter of the collecting dish) inherent to long wavelengths (= radio waves). [42] Many objects in the universe, such as stars, galaxies, nebulae, pulsars, quasars but also planets, emit radio waves. [43]

The radio frequency regime ranges from several kHz up to approx. 3 GHz ($\lambda \approx 100$ km down to ≈ 10 cm). Short wavelengths are absorbed in the atmosphere, long wavelengths are reflected from the ionosphere. These limits define the window of observable radio waves for ground-based detection.

The physical processes responsible for the continuum emission (in contrast to line emission from atomic processes with quantized energies) of radio waves can either be thermal or non-thermal. Both types result from accelerations of charged particles. Thermal emission only depends on the temperature of the source. All bodies with temperatures above 0 K emit electromagnetic radiation due to the internal (accelerated) particle motion. The ideal case of thermal emission is that of a black body. Non-thermal emission is produced when charged particles spiral around magnetic field lines. On their helical paths the particles experience an accelerated motion that results in electromagnetic emission. In the non-relativistic case this is known as cyclotron radiation. On the other hand synchrotron emission occurs when the particles travel with velocities close to the speed of light. Then the energy emitted not only depends on the magnetic field strength as for cyclotron radiation but also on the energy of the charged particles. Non-thermal emitters show polarization in contrast to thermal sources, which are generally not polarized.

Usually a parabolic shaped reflector used to focus the radio waves onto an antenna is referred to as a radio telescope. The larger the reflecting surface the greater the amount of energy gathered. Weak radio signals can so be detected. The collected radio signals are then converted into electrical voltages which are amplified. These signals can then be processed and displayed. A single-dish radio telescope collects all the radio energy from a small area in the sky. This area is called beam and defines the resolution of the telescope, which depends on the observed frequency and the diameter of the dish. Better resolution can be achieved by increasing the diameter and by observing higher frequencies. Increasing the resolution by larger and larger dishes reaches a structural limit at some point so that the dish does not collapse. Another way of improving the resolution is the use of interferometry. A larger collecting facility can be simulated by combining the signals received by several locally separated telescopes; this technique is called aperture synthesis. The resolution is then determined by the distance between the individual dishes.

The dish type radio telescopes are predominantly used for shorter wavelengths (= high frequencies). In the low frequency regime (f = 10 - 100 MHz, λ = 30 - 3 m) directional antennas are employed. Radio telescopes can thus consist of either single dishes, a combination of several dishes or large collections of mere dipole/directional antennas (= arrays).

When an array is used as an interferometer, signals from pairs of antennas are corre-

lated. The phase and contrast of the resulting interference fringes are associated with the Fourier transform of the spatial distribution of the source intensity. The Fourier coefficients (u,v) describe the spatial (angular) frequencies of the interference pattern and are never fully determined. The intention of aperture synthesis is to fill the plane spanned by the Fourier coefficients (u,v) as completely as possible. A high-quality image can then be obtained by transformation back into image space and deconvolution to clean the image from undesired side lobes that come from incomplete (u,v)-coverage. [42, 43]

Basically, radio-astronomical observations can be carried out around-the-clock, however, best quality can be achieved during night due to lower disturbance from radio broadcasting, citizen band, radars, etc.

2.14 Radio astronomy instrumentation

Various types of radio telescopes have been used in the radio astronomical research of planets and other objects in the decametre wavelength regime. Several ground-based systems for the study of this low frequency regime ($f < 100$ MHz) are available in Europe, where a lot of data on Jupiter radio phenomena was collected. Numerous results have been obtained by the Ukrainian T-shaped radio telescope, second modification (UTR-2), Ukrainian Radio Interferometer of NASU (URAN) and the Nançay Decametric Array (NDA) in France. These long-serving and large devices meet the requirements for high quality investigations. They are utilized in planetary and solar studies and provide the basis for the development of new instruments.

The new radio telescope systems feature a substantially larger number of stations, which improves their imaging capabilities. Together with larger numbers of elements, larger effective areas and wider frequency ranges high-level experiments will be performed in the near future. The new generation of low frequency radio telescopes comprises the Low Frequency Array (LOFAR) and the LOFAR Outrigger in Scandinavia (LOIS) as well as its American counterpart, the Low Wavelength Array (LWA) in New Mexico, USA. The LOFAR is already being enhanced to form the New Extension in Nançay Upgrading LOFAR (NenuFAR), which will serve as a pathfinder for the huge Square Kilometre Array (SKA) project [44]. The construction of SKA in South Africa and Australia is scheduled to start in 2018. First results from this array with a collecting area of approx. one square kilometre are expected in the early 2020s [45]. Also UTR-2 is expanded in frequency range (8 - 80 MHz) and spatial dimension to form the Giant Ukrainian Radio Telescope (GURT) in order to participate in joint international observation campaigns. [46]

Beyond that, space-based missions concentrate on phenomena that cannot be studied on Earth because of the ionospheric cut-off or the protection of the magnetosphere from the solar wind (Solar Terrestrial Relations Observatory (STEREO), Solar Imaging Radio Array (SIRA), etc.).

One focus of low frequency radio astronomy lies on solar system radio astronomy. This includes the study of the Sun and the planets. The results of these fundamental investigations can be transferred to other objects in the universe, as the physical processes and generation mechanisms are universally valid. The studied objects involve the planets (particularly Jupiter), the Sun with its bursts and coronal mass ejections (CME), the interplanetary medium, the Moon, comets, exoplanets, flare stars, pulsars and the unknown sources of sporadic decametre radiation.

Figure 11 illustrates the wide field of objects being studied by the UTR-2 and URAN telescopes. The NDA is mainly used for Sun and Jupiter investigations [47]. These fields are extended by the operation of LOFAR/NenuFAR and LWA.

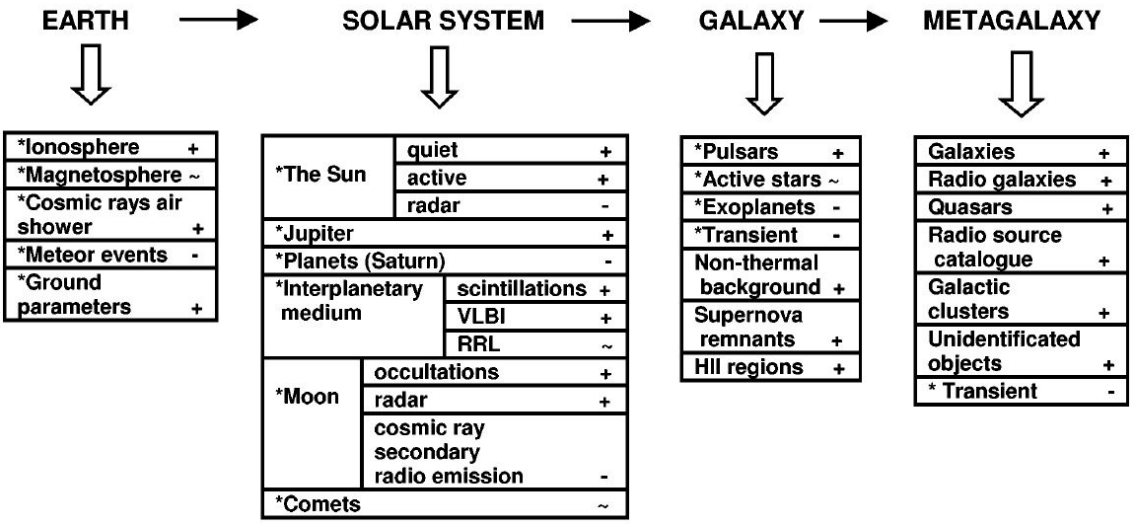

Figure 11: Objects investigated with UTR-2 and URAN. (+) marks the fields with positive results for a large amount of investigated objects; (∼) stands for a rather limited number of results. For the (-) objects no results have been obtained so far. For the objects marked by (*) the confusion effect (describes stochastic fluctuations of the background sky brightness below which sources cannot be detected individually [48]) does not restrict the sensitivity. [49]

The Very Long Baseline Interferometry (VLBI) system URAN was built on the base of the UTR-2 array, which offers a large maximum effective area of 150000 m^2. URAN consists of UTR-2, URAN-1, URAN-2, URAN-3 and URAN-4. URAN-1 and URAN-4 are part of the Institute of Radio Astronomy, URAN-2 belongs to the Gravimetric Observatory of the National Academy of Sciences of Ukraine (NASU) in Poltava and URAN-3 is operated by the Institute of Physics and Mechanics of NASU in Lviv [7]. The system offers several baselines from 40 to 950 km [50]. The distribution of the URAN telescopes in Ukraine is displayed in Figure 12.

The data used in this thesis comes from the URAN-2 telescope (see Figure 13) which is operated in a frequency range from 8 to 32 MHz. The antenna array of URAN-2 has an effective area of 28000 m^2 and consists of 512 crossed-dipoles. The beam pattern size at 25 MHz is 3.5×7 deg. The sensitivity is estimated to be 100 Jy. [51] The telescope is able to measure linear and circular polarization of radio signals. Since 2005 URAN-2 performs regular monitoring of solar radio emissions. Since September 2012 Jovian radio emissions are observed. [19]

Table 3 lists the main parameters of UTR-2, the URAN telescopes and NDA.

Figure 12: Distribution of URAN telescopes in Ukraine [7]

Figure 13: URAN-2 telescope in Poltava, Ukraine [52]

Table 3: Main parameters of selected decametre wavelength radio telescopes [49]

Radio telescopes	Location	Frequency range/MHz	Maximum effective area/m^2	Number of elements, polarization	Angular resolution at 25 MHz
UTR-2	Kharkov, UKR	8 - 32	150000	2040, 1 linear	25' x 25'
URAN-1	Zmiev, UKR	8 - 32	5500	96, 2 linear	60"
URAN-2	Poltava, UKR	8 - 32	28000	512, 2 linear	21"
URAN-3	Lviv, UKR	8 - 32	14000	256, 2 linear	2.7"
URAN-4	Odessa, UKR	8 - 32	7300	128, 2 linear	4.0"
NDA	Nançay, FRA	8 - 88	2x4000	2x72, 2 circular	$\approx$ 1.0"

Observing narrow-band and short-time processes requires high frequency and time resolution. A high signal-to-noise ratio can thus only be achieved by large effective areas. Furthermore, the large area in combination with high antenna directivity increases the signal-to-interference and the signal-to-signal ratio (traceability of fine signal structure against the background). Both are important for the detection of decametre radiation. This emission is especially susceptible to natural and artificial interferences. The influences of the ionosphere, the interplanetary and interstellar medium are extremely strong. Thus the radio waves are absorbed, refracted and scattered. Moreover, the brightness temperature of the non-thermal galactic radio emission is high. These difficulties have to be overcome by the application of special methods and equipment.

The outstanding results achieved by low frequency ground-based radio astronomy compensate for the challenge to obtain high quality data in this field. Ideas exist to install low frequency radio instruments into outer space or on the moon to avoid the negative influences of the Earth's ionosphere. On the other hand building large effective areas in space is almost impossible to realize. Thus the development of a new generation of low frequency telescopes on Earth, such as LOFAR/NenuFAR and SKA, remains indispensable. At the same time the capacity of operational systems has to be fully utilized to guarantee excellent research results in future. [7, 49]

2.15 Zebra spectral structures

Zebra spectral structures have already been observed in radio spectra of the Sun and in lower frequency ranges of Jupiter. First sightings of zebra structures in solar radio spectra have been reported by Elgarøy in 1959 [53] where they appear as bright and dark stripes superposed on the background burst [54]. Solar radio astronomy developed in the 1940s and has since grown into a large scientific branch. Solar radio bursts were classified into 5 distinctive types. Especially the type IV bursts feature a rich variety of fine structures. Stripes that appear in these bursts were divided into fibre bursts and zebra patterns, which are sometimes difficult to distinguish. The name zebra pattern was introduced in 1972 as it appeared most appropriate for the observations. The study of the fine structures of the solar radio emission is essential for the comprehension of plasma processes in the solar corona.

Figure 14 shows one of the first observed solar zebra patterns with their basic properties: preferred drift to high frequencies, occasionally the stripes are not parallel, the frequency separation between stripes increases with frequency and the frequency drifts can even change abruptly. So far zebra stripes have been reported between 20 and 6000 MHz. Zebra events feature between 5 and 20 individual stripes (even up to 70 stripes), the stripe spacing at 160-200 MHz is approx. 2-3 MHz, at 800-900 MHz intervals of 20 MHz have been recorded. Most events are emitted in ordinary mode as a modulation of the strong circularly polarized continuum emission. [55]

During Cassini's flyby of Jupiter on its way to Saturn in 2000/2001 detailed observations of low frequency Jovian radio emissions were performed. Among the most enigmatic phenomena observed were the kilometric bursts (frequencies below 100 kHz) that consisted of several parallel stripes in the dynamic spectra. Such an event can be seen in Figure 15 where 5 emission stripes in the frequency range from 30 to 70 kHz are displayed. Irregular frequency changes of the stripes can be observed, while they remain almost parallel to

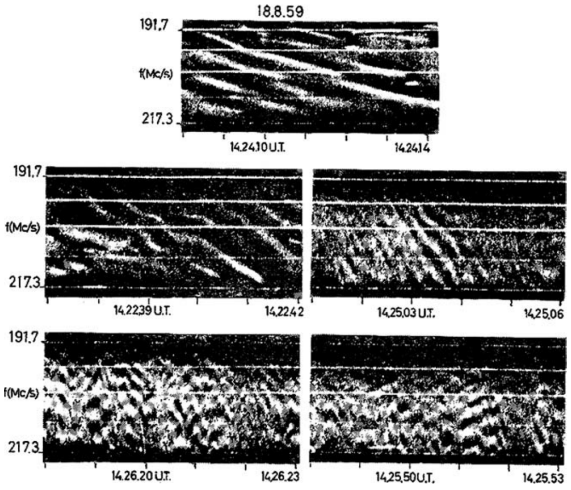

Figure 14: An example of solar zebra structures in the event August 18, 1959. [56] The unit megacycles per second (Mc/s) is an out-dated name for the frequency unit megahertz (MHz).

each other. The stripes are not exactly equidistant; that has also been reported for solar zebra stripes. Generally, the frequency intervals between the adjacent stripes slightly increase with the emission frequency. These intervals and the number of stripes vary with time. In the beginning of the event (at 02:58:40 - 02:59:40 spacecraft event time (SCET)), short quasi-periodic bursts with very fast frequency drift are superposed on weak striped structures. The intensity is about two orders of magnitude higher compared to the usual intensity of Jovian radio emission at these frequencies. [12]

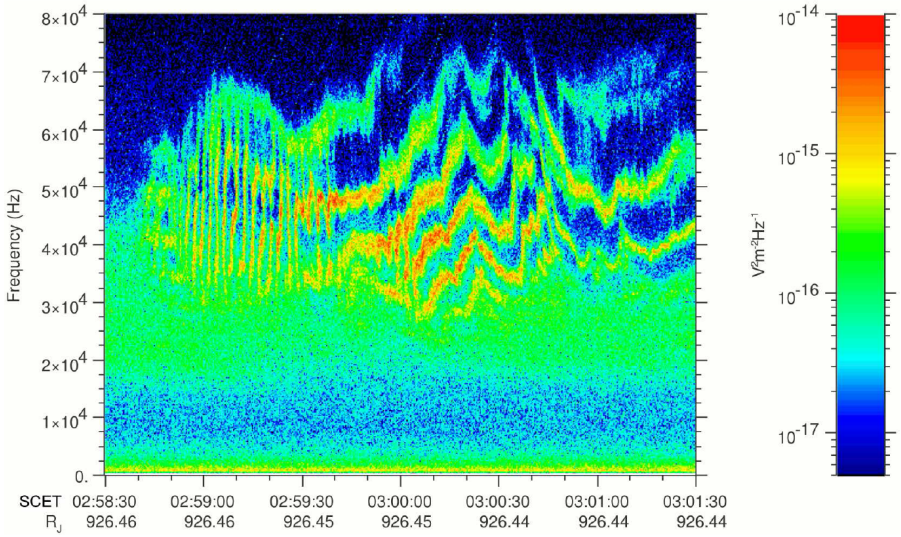

Figure 15: Dynamic spectrum of Jovian radio emission recorded by Cassini on Oct 21, 2000 (courtesy of W.S. Kurth, Cassini RPWS Team, University of Iowa). [12]

Many mechanisms have been proposed to explain the (solar) zebra phenomenon. The most developed model is based on the Double Plasma Resonance effect which is introduced in section 2.3.

3 Data Acquisition

Zebra patterns have been registered in the dynamic spectra of Jupiter by the ground-based radio telescope URAN-2, Poltava, Ukraine. This telescope is among the largest low frequency telescopes in Europe. For more details on radio astronomy and its instrumentation see sections 2.13 and 2.14.

Table 4: Jupiter radio emission observation campaigns

Campaign	Start	End	Observations	Episodes
#1	18 Sep 2012	23 May 2013	18	13
#2	21 Aug 2013	31 Mar 2014	24	21

Two observation campaigns at URAN-2 provide the data for this study (see Table 4). The data is recorded in a broad frequency range from 8 to 32 MHz with high frequency and time resolution (4 kHz and 100 ms). 86 preselected dynamic radio spectra with a duration of 30 minutes are visually scanned for probable zebra events. In these dynamic spectra intensity is displayed as a function of time (x-axis) and frequency (y-axis). The shading/colour reflects the intensity in dB-scale above background. For more details see section 2.4 and especially sections 2.5, 2.6 and 2.8 for disturbing effects that can be found in the dynamic spectra.

Structures consisting of individual quasi-parallel stripes over a larger frequency range that drift in a time frame of several minutes and also appear in the polarization spectrum, indicate a potential zebra event (Figure 16). These structures are then enlarged and displayed in high resolution in colour with the Spectra Viewer V15 tool and thoroughly analysed. This tool includes the background correction. The calibration file contains all measured noise (e.g. from internal sources or inaccurately aligned antennas) which is subtracted from the signal while taking the frequency dependence of the noise into account.

The 42 most distinctive events in terms of high resolution and intensity are selected for detailed statistical analysis. The rather small sample size requires careful treatment in order to draw the right conclusions from the data available.

Occasionally zebra events appear sequentially within a couple of minutes. Such events are combined into *episodes*. Thus, the statistics of distribution are not distorted by events that occur at the same Central Meridian Longitude (CML) or Io phase position and are evidently connected. The 34 episodes can include several single zebra structures. The grouping into episodes only applies to the CML and Io phase distributions. For interpreting the frequency properties of the zebra phenomenon this classification is not necessary.

Each zebra event is characterized by the exact date and time, the number of lines of the structure and its polarization as well as the CML (see section 2.1) and Io phase (see section 2.9) coordinates of the telescope during the observation. The run of the individual zebra stripes is recorded to allow the study of the frequency properties, especially the frequency range of occurrence and the frequency splitting between single stripes. Figure 17 illustrates the characterization process. The event was recorded on Nov 10, 2012 between 23:46:15 and 23:49:30 UT in the frequency range from 20 to 27 MHz. Overall 9 stripes were recorded. Note that not all of them appear simultaneously and that their frequency

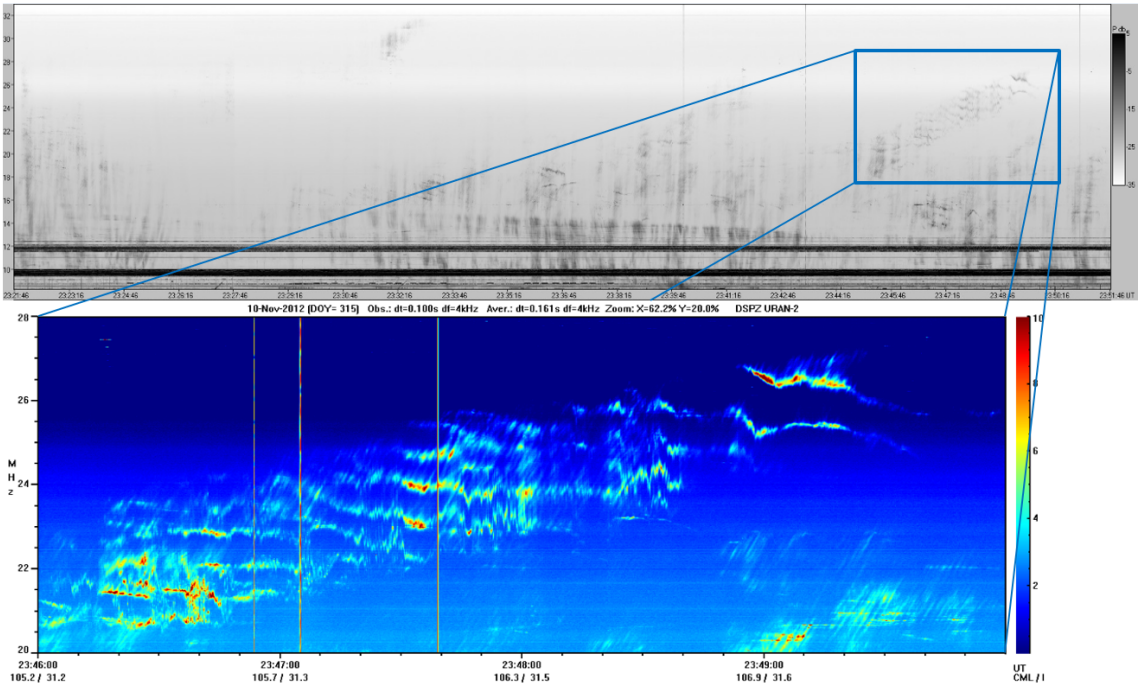

Figure 16: Process of finding a zebra event. First, overview spectra are scanned visually for probable structures (marked by blue box). These structures are then enlarged and displayed in high resolution in colour with the Spectra Viewer V15. This tool also allows measuring the frequency properties of the zebra event.

properties fluctuate during the course of the event, which lasted about 3.5 min. The event was RH polarized (the polarization measurement is not shown in this figure) and occurred at approx. 106° CML and an Io phase of about 31.5°. The red bars in Figure 17b depict the determination of the frequency data.

Figure 18 shows two additional examples of zebra events including the polarization spectrum of one event. Here (Figure 18c) the colour denotes the sense of polarization, blue for RH and red for LH polarized emission. The event in Figure 18a was observed on Oct 28, 2013 between 23:46:30 and 23:50:30 UT. 4 stripes appeared within 4 minutes between 17 and 23 MHz at approx. 136° CML and 344° Io phase in RH polarization. The intensity is slightly stronger than for the Nov 10, 2012 event (Figure 17). Figure 18b provides another sample. This zebra pattern was registered on Jan 01, 2014 between 21:59:45 and 22:00:30 UT with 6 stripes in a frequency interval of 15 to 18 MHz. The CML was 142° and the Io phase 240°. Compared to the two previously discussed events the intensity of this event is significantly higher (note the different colour scales). Moreover, Figure 18c displays the polarization spectrum. The blue colour indicates RH polarization.

The outlined procedure was repeated for all 42 selected zebra events. The results of the subsequent statistical analysis should eventually provide the basis for the theoretical framework of the Jovian zebra phenomenon.

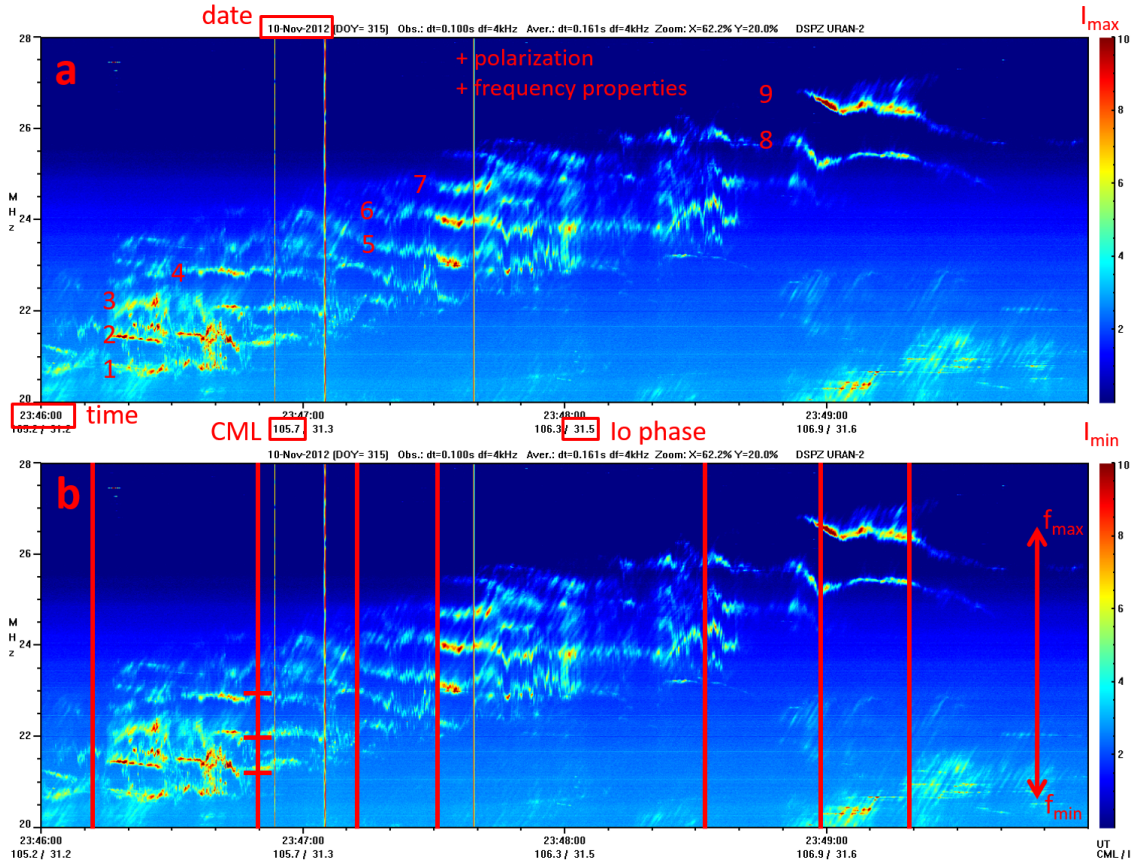

Figure 17: Characterizing a zebra event. a) Exact date and time, the CML and Io phase, the number of lines of the structure and its polarization are recorded. b) The red vertical lines mark the points of time where the frequencies of the stripes are recorded (exemplarily shown by the 3 slim horizontal lines). Also the overall frequency range of the event is recorded, i.e. the minimum and maximum frequency value of the event.

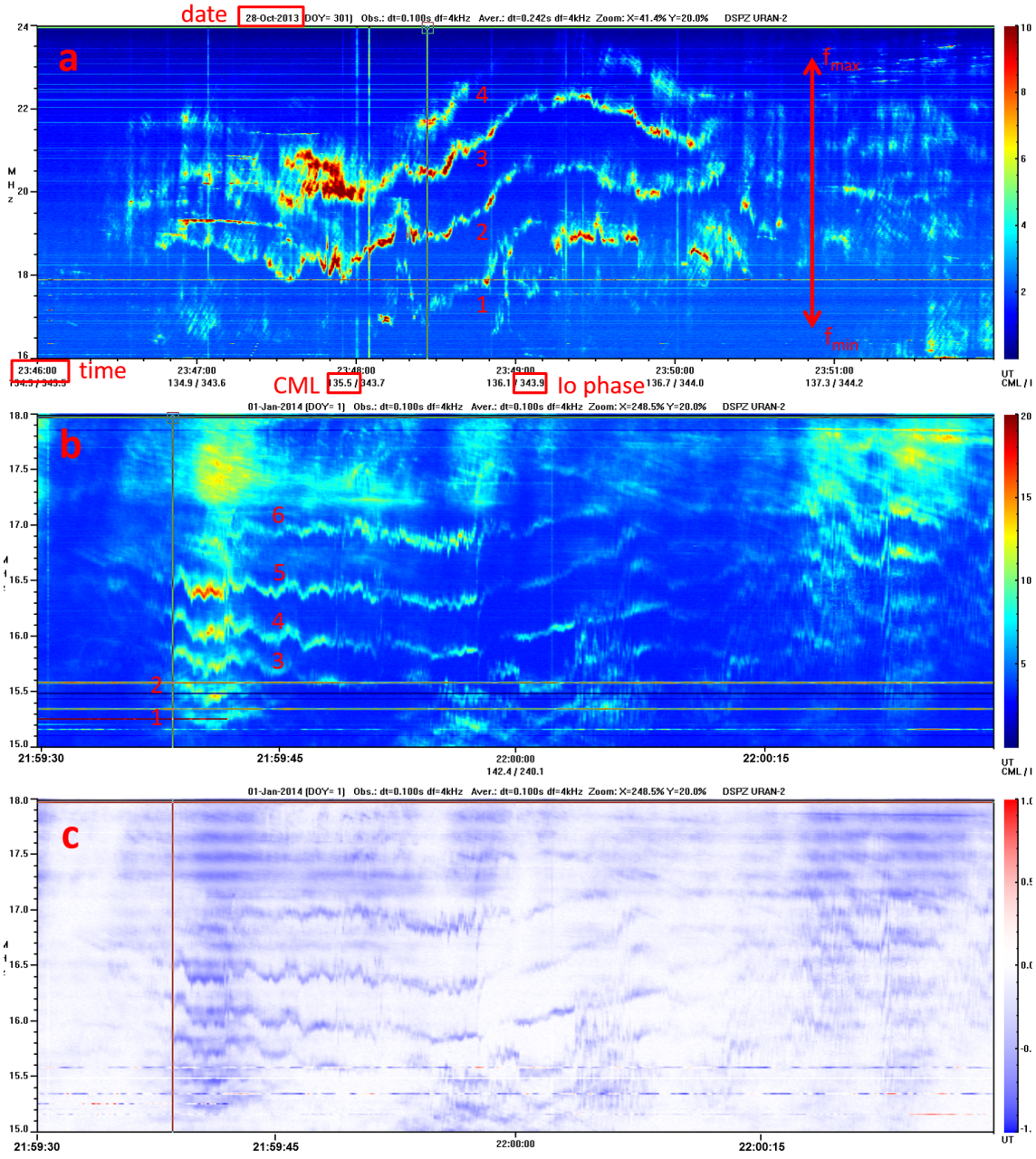

Figure 18: Dynamic spectra of zebra events. a) and b) are two additional examples of intensity coded spectra. Several properties of the events are marked in red, the zebra stripes are counted. c) shows the polarization spectrum of the event in b). Here the colour displays either right-handed (blue) or left-handed (red) polarization.

4 Data Analysis

The statistical analysis of the data retrieved from the dynamic spectra (described in chapter 3) should eventually provide the basis for the theoretical framework of the Jovian zebra phenomenon. The two observation campaigns from September 2012 until March 2014 at the large ground-based radio telescope URAN-2 in Poltava, Ukraine, resulted in 42 zebra events that are subsequently studied in detail. The study requires careful handling due to the rather small sample size.

The statistical analysis is carried out in MATLAB and comprises the following aspects:

- occurrence distribution of zebra structures as a function of Io phase
- occurrence distribution as a function of CML
- distribution of sense of polarization
- distribution of polarization in respect of the date
- distribution of RH polarized episodes as a function of CML and Io phase
- distribution of LH polarized episodes as a function of CML and Io phase
- frequency properties of the zebra structures, including minimum and maximum observed values, frequency ranges and frequency spacings.

4.1 Occurrence distribution as functions of Io phase and CML

In the first step of analysing the Jupiter zebra structures the occurrence distributions are studied as functions of Io phase and CML. The idea is to find out whether the phenomenon is driven by the satellite Io. Jupiter's radio emission is known to be influenced by its moon in several aspects. On the other hand, the structures can be localized with the CML measurement. A dependence on the longitude could point to active regions on Jupiter where the emission of zebra structures is more likely. See chapter 2 for more information on the fundamentals.

The corresponding histograms with box sizes of 20° can be seen in Figure 19. Here the distributions of *episodes* of zebra events are displayed. Zebra events that appear sequentially within a couple of minutes are registered as one episode. Thus, the statistics of distribution are not distorted by events that occur at the same CML or Io phase position and are evidently connected. The 42 zebra events are grouped into 34 episodes.

The tilted panel on the left in Figure 19 shows the Io phase distribution of zebra episodes. No influence of the Io phase can be detected as no Io phase value exhibits a significant larger number of zebra occurrence. Therefore it can be concluded that zebra structures are not controlled by Io. This fact can be substantiated by comparing the Io phase distribution to the well-known Io related and non-Io related sources diagram (overall Figure 19; see section 2.7 for more details). The Io phase distribution of the episodes does not correspond to any known Io source. The zebra structures are a non-Io related phenomenon!

The lower panel in Figure 19 displays the distribution of zebra episodes as a function of CML. In contrast to the rather uniform Io distribution two regions in the CML range feature significantly larger numbers of episodes: from 300° to 60° and from 100° to 160° CML. This indicates two active regions of CML on Jupiter where the zebra patterns are more

likely to occur. These two active regions will be referred to repeatedly throughout the following investigations as they play an important role in the characterization of the zebra phenomenon.

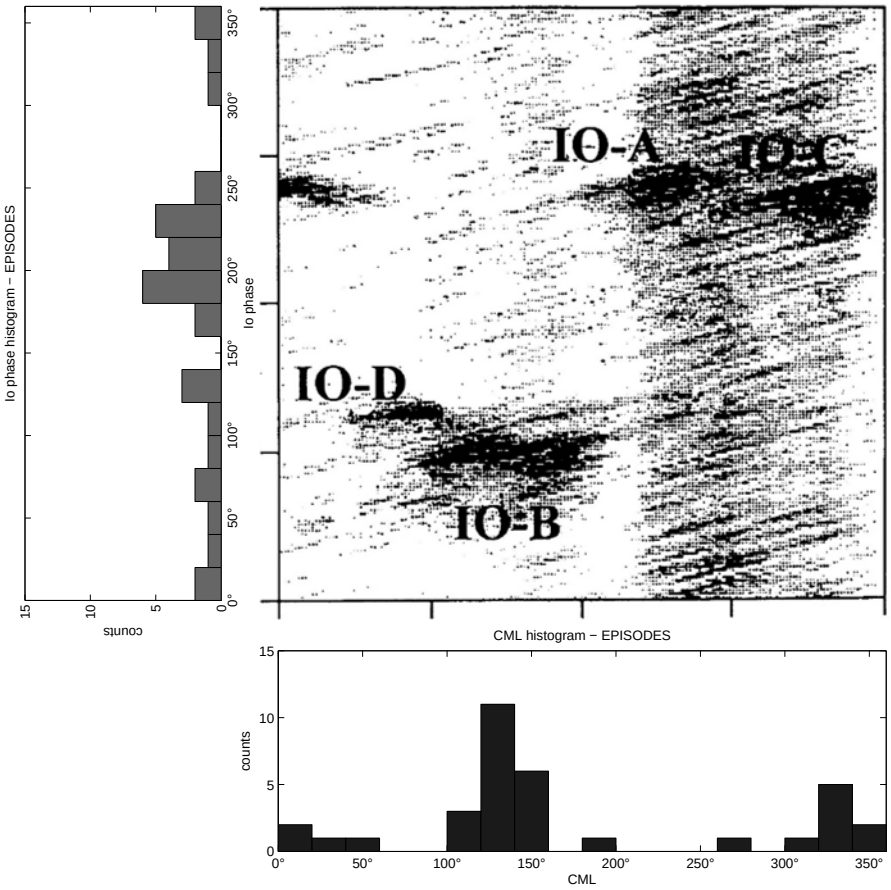

Figure 19: Comparison of zebra Io phase and CML distributions to the well-known Io related and non-Io related sources diagram. The left panel (tilted, grey bars) shows the histogram of Io phase distribution. The lower panel illustrates the CML distribution. Both histograms reflect the distribution of episodes of zebra events with box sizes of 20°. The figure in the centre (from [23]) displays the occurrence of DAM as functions of CML and Io phase by black shading. The Io-A, Io-B, Io-C and Io-D sources are labelled.

4.2 Polarization

The observed zebra events are highly elliptically polarized. Classifying the zebra events into their sense of polarization offers another possibility to localize the zebra structures. By assuming the emission to be in RX-Mode it is possible to determine the source region of the zebra stripe emission. RH polarized radiation can be allocated to the northern hemisphere of Jupiter and LH polarized radiation to the southern Jovian hemisphere (see section 2.12). The division into RH and LH polarized events also reveals the distribution of the events: 24 are RH, 18 are LH polarized. See Figure 20 for the pie chart. No clear tendency to one sense of polarization can be found; RH polarized events marginally predominate. This fact could to some extent be attributed to the Jovicentric declination of Earth (D_e). The declination coordinate of Earth as seen from Jupiter varies between -3.3° and +3.3° during Jupiter's orbit around the Sun (approx. 11.9 years) [57]. During the two observation campaigns the position of the observer in the Jovian coordinate system hardly varied (89.84° to 90.03°) and the northern Jovian hemisphere was facing the Earth slightly more than the southern hemisphere. This may explain the slight dominance of RH polarized events. Moreover, the polarization of the events is not linked to certain periods of time. Neither LH nor RH polarized events appear more often in a certain time span as illustrated in Figure 21, where the two observation campaigns are presented separately.

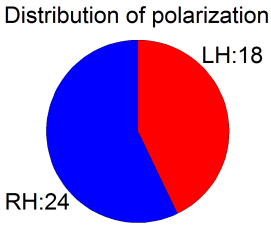

Figure 20: Pie chart of the distribution of the sense of polarization of the 42 registered zebra events. 24 events are RH (blue), 18 LH polarized (red).

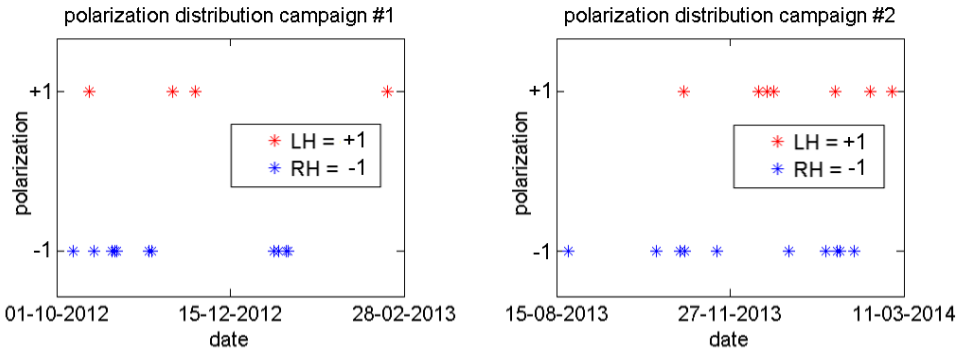

Figure 21: Occurrence of RH (blue) and LH (red) polarized episodes as a function of time. The left panel shows the first observation campaign from 09/2012 till 05/2013, the right panel the second campaign from 08/2013 till 03/2014. The value -1 represents the RH polarized episodes drawn in blue. Value +1 stands for the LH polarized episodes in red. Note that some markers may overlap, particularly for the RH polarized cases.

An exciting fact is revealed by separately visualizing the CML dependence of LH and RH polarized episodes in order to pinpoint the source region of the zebra structures. Figure 22 shows 3 histogram panels. The top panel represents the CML distribution of all zebra episodes (black). The middle panel shows the RH polarized episodes (blue), the lower panel displays the LH polarized cases only (red). Apparently the two CML regions where zebra patterns occur can be assigned to a specific sense of polarization: the range from 100° to 160° is related to RH polarization, the region from 300° to 60° CML provides LH polarized zebra events. The colored histograms in Figure 22 clearly show the two separate source regions on the northern (RH polarized) and on the southern (LH polarized) hemisphere with their corresponding zone of occurrence of CML. It should be noted that the maxima of the RH and LH polarized distributions are separated in CML by approx. 200°. This will be important for later considerations on the Jovian magnetic field (see section 5.1).

The exceptions to the two CML regions (two for RH and two for LH, see Figure 22) are listed in Table 5. Here the exact measured CML and Io phase values for the episodes are given. Two episodes were observed after strong Io incidents. It cannot be ruled out that those Io-related emissions overlap the zebra events. Io-A sources emit RH polarized radiation and could therefore cover a weaker LH polarized zebra event at 278° CML. The same could possibly apply to the zebra episode that occurred together with an Io-D emission. Io-D is LH polarized and could have overlapped a fainter RH polarized zebra episode at 135° CML. The two other outlier episodes cannot be related to any particular disturbance. The deviation happened most probably accidentally. Full clarification requires further investigations.

Table 5: Exceptions to the two CML regions

Polarization	CML	Io phase	Date	Time	Note
RH	278°	197°	26 Oct 2012	21:19 - 21:21	Io-A
RH	334°	350°	17 Oct 2012	00:43 - 00:48	
LH	135°	136°	15 Oct 2012	23:24 - 23:38	Io-D
LH	191°	199°	23 Dec 2013	21:00 - 21:16	

Figure 23 once more emphasizes the non-Io related character of the zebra structures visualizing the Io phase dependence of LH and RH polarized episodes. The top panel represents an overview including all zebra episodes (framed in black). The middle panel shows the RH polarized episodes (blue frame), the lower panel displays the LH polarized cases only (red frame). Also in this separate presentation relating to polarization a dependence of the zebra structures on the Io phase cannot be derived.

In summary, the zebra phenomenon is merely governed by CML. Two active regions on Jupiter can be accounted for. By knowing the sense of polarization of the zebra event it is possible to forecast the source region of the zebra event as the sense of polarization determines the hemisphere and the region of CML:

- RH → north + 100° - 160° CML
- LH → south + 300° - 60° CML (through 360°)

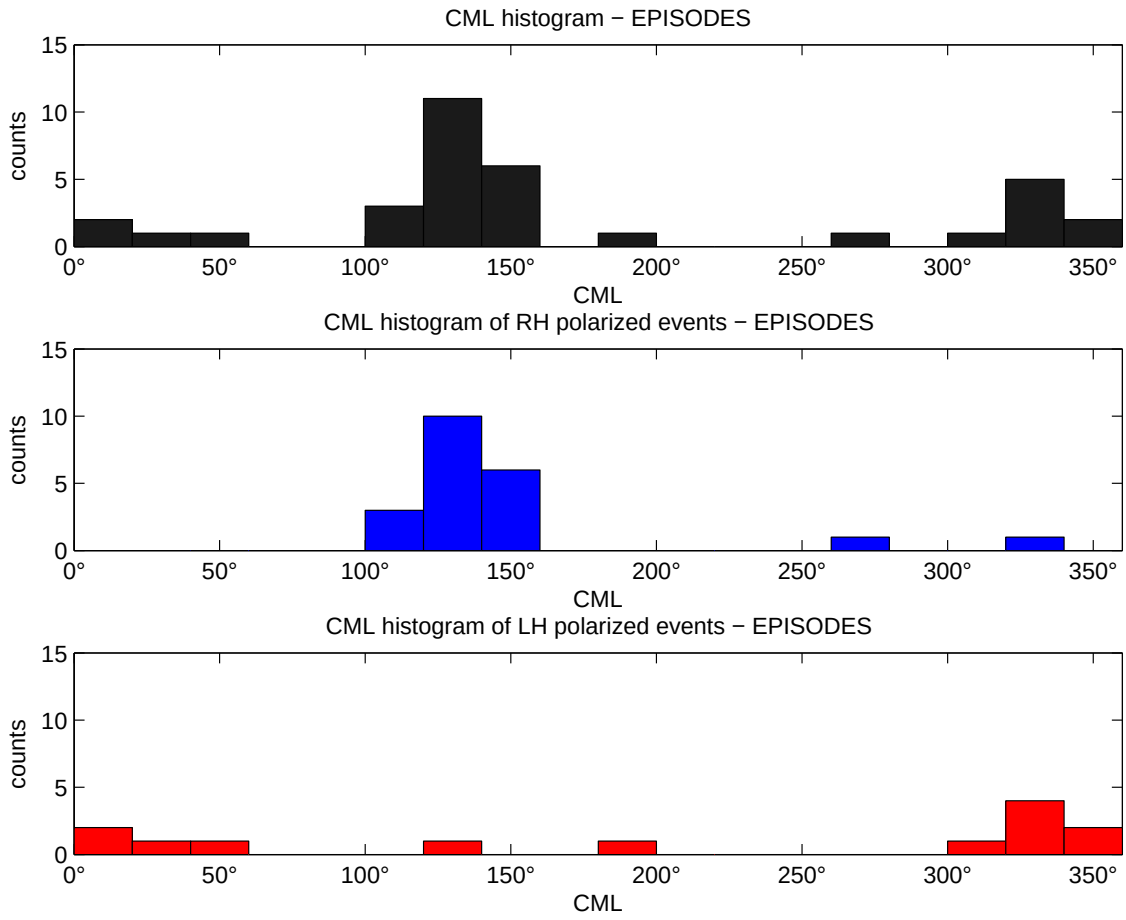

Figure 22: Histograms of the distribution of zebra episodes as function of CML. The top panel is the same as in Figure 19 and serves as an overview histogram displaying all zebra episodes (black). The middle panel shows the RH polarized episodes only (blue), the lower panel displays the LH polarized cases (red). "Adding up" the RH and LH distribution yields the black overall distribution. The box size is 20°.

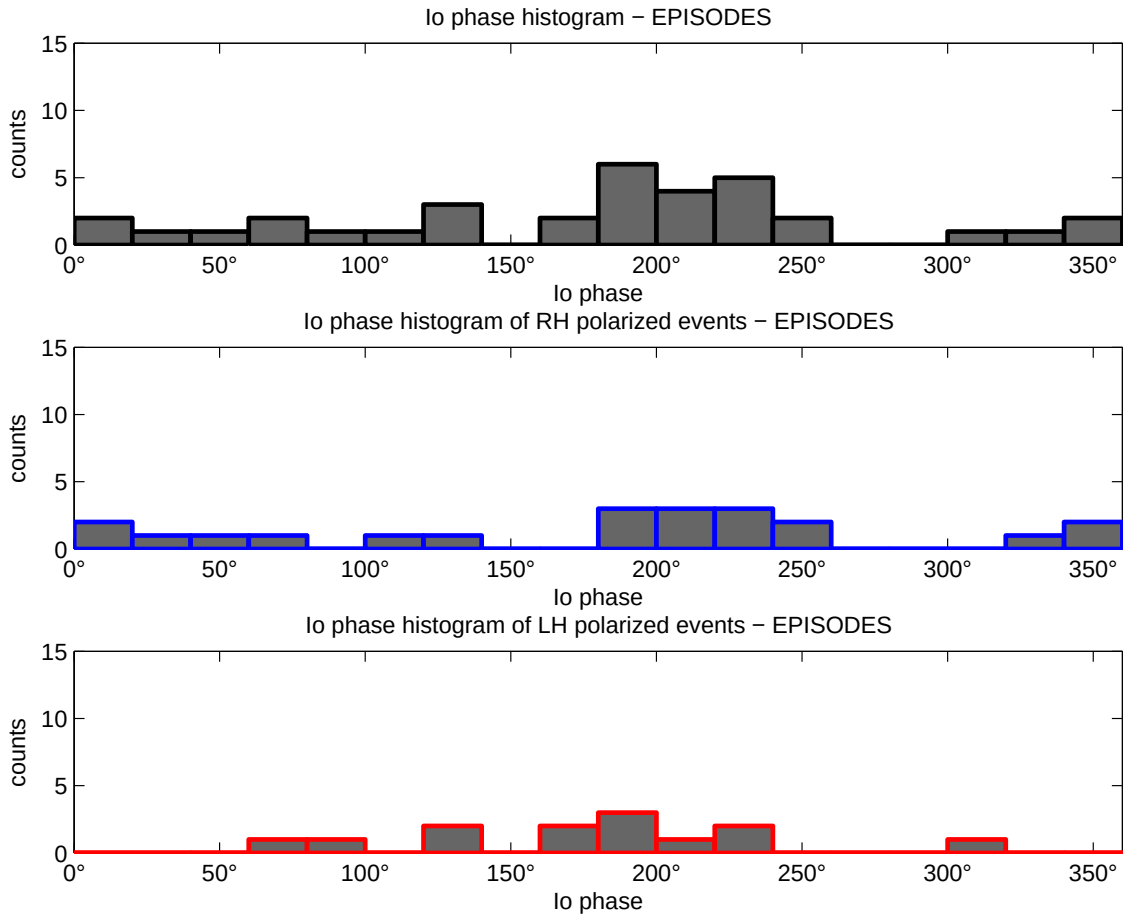

Figure 23: Histograms of the distribution of zebra episodes as function of Io phase. The top panel is the same as in Figure 19 and serves as an overview histogram displaying all zebra episodes (black frames). The middle panel shows the RH polarized episodes only (blue frames), the lower panel displays the LH polarized cases (red frames). "Adding up" the RH and LH distribution yields the black framed overall distribution. The box size is 20°.

4.3 Frequency properties of zebra spectral structures

Analysing the frequency properties of the Jovian zebra events should help shedding light on the mechanism that controls the phenomenon and relating it to similar processes that have already been observed at the Sun and in lower frequency ranges at Jupiter (see section 2.15). The grouping into episodes is irrelevant here. The frequency properties are retrieved from every single zebra stripe which is independent of its relation to other zebra events that appear close in time.

An overview of several frequency properties can be seen in Table 6. These parameters are explained and discussed below. The zebra events occur in an overall frequency range from 12.5 MHz $\leq f \leq$ 29.7 MHz. These limits represent the lowest detected frequency f_{min} and the highest observed frequency f_{max}. In average one zebra event extends over $\overline{f}_{range} = 2.8 \pm 1.5$ MHz. Another interesting parameter is the frequency spacing Δf between two neighbouring stripes. The minimum value is $\Delta f_{min} = 0.2$ MHz, the maximum recorded value $\Delta f_{max} = 3.7$ MHz. The mean frequency spacing averages out at $\overline{\Delta f} = 0.8 \pm 0.4$ MHz. The bandwidth df of one stripe varies between 0.1 MHz $\leq df \leq$ 0.4 MHz; the majority of stripes shows bandwidths between 0.1 and 0.2 MHz. The bandwidth is therefore clearly less than the frequency spacing Δf: $df \ll \Delta f$. Several frequency properties are summarized and visualized in Figure 24.

Table 6: Frequency properties of zebra events in MHz

f_{min} ... minimum observed frequency
f_{max} ... maximum observed frequency
$\overline{f}_{range}$ ... mean frequency range for one event
Δf_{min} ... minimum frequency spacing
Δf_{max} ... maximum frequency spacing
$\overline{\Delta f}$ ... mean frequency spacing

f_{min}	f_{max}	$\overline{f}_{range}$	Δf_{min}	Δf_{max}	$\overline{\Delta f}$
12.546	29.710	2.777 ± 1.530	0.190	3.712	0.760 ± 0.411

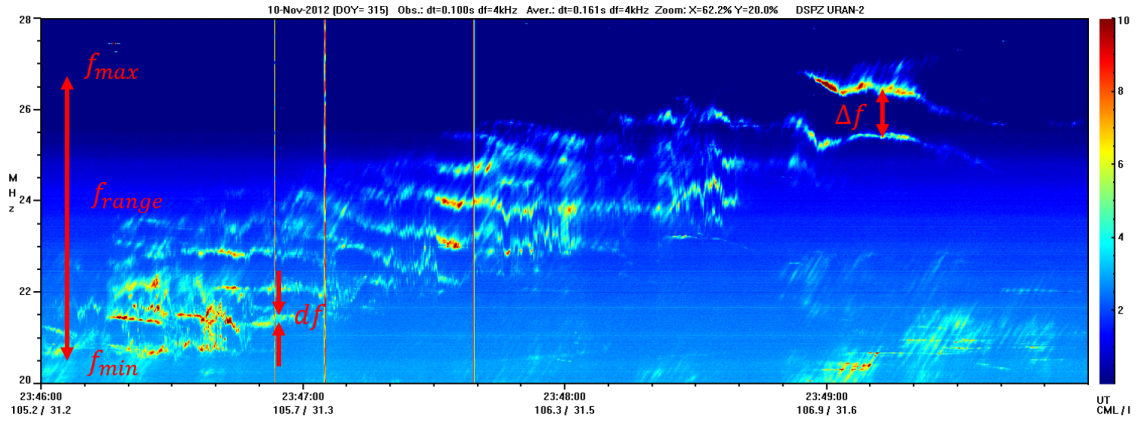

Figure 24: Visualization of the frequency properties of zebra events

The distribution of frequency spacings Δf between neighbouring stripes can be seen in Figure 25. As already pointed out, the frequency spacing ranges from 0.2 to 3.7 MHz with an average of $\overline{\Delta f} = 0.8 \pm 0.4$ MHz. The spacing between two actually neighbouring stripes is not always fully retrievable from the observations. In some cases there might exist stripes in between that do not appear in the spectra because their intensities are too low. This certainly applies for the cases with spacings larger than 3 MHz in the histogram. Also the average value of the frequency spacing is deceiving. It should only serve as a reference value to get an idea of the spacing in general. Actually an increase of the frequency spacing with increasing frequency can be observed. For 72 % of the stripes the distance to the next stripe increases the higher in frequency the stripes occur (also reported for solar and Jovian KOM zebra patterns, see section 2.15). This fact is illustrated by the pie diagram integrated in Figure 25, where white stands for the increase of Δf and grey for the decrease.

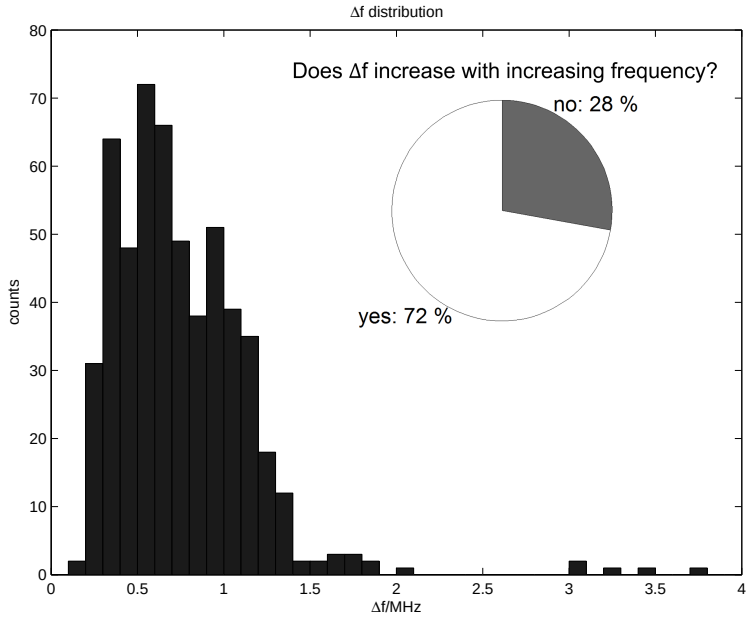

Figure 25: Histogram of the distribution of frequency spacings Δf between two neighbouring stripes. The box size is 0.1 MHz. In the upper right corner the pie chart answers the question "Does Δf increase with increasing frequency?". For 72 % of zebra stripes (white) this can be answered "yes", for 28 % with "no" (grey).

The middle panel in Figure 26 shows the frequency ranges of the 42 zebra events as a function of CML. One bar denotes one event. The lower marker of the bar represents the minimum frequency in the lowest stripe, the upper marker indicates the highest recorded frequency in the highest stripe of the event. Moreover, the events are categorized into their sense of polarization by colour (blue: RH, red: LH polarized) as in the histograms in Figure 22. Events that are spread over a wider frequency range feature a larger number of individual stripes. Such events predominantly appear in the CML interval between 100° and 160°. As mentioned in section 4.2 this is the interval where primarily RH polarized events occur which in addition means that the radiation emerges from the northern Jovian hemisphere. The two panels on the left and right illustrate the distribution of minimum and maximum frequency values of the LH (red) and RH polarized (blue) events.

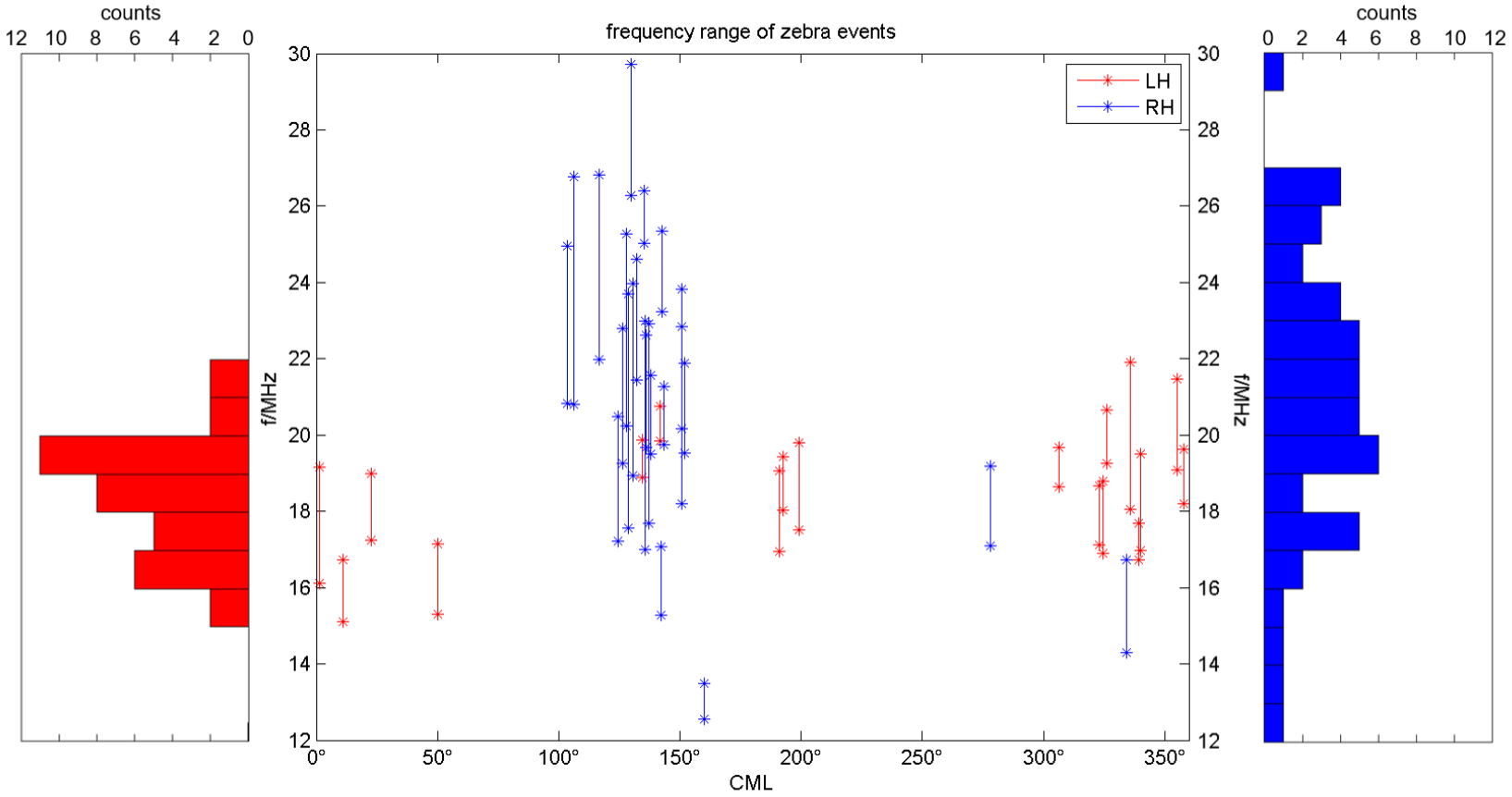

Figure 26: Centre: Frequency range of LH (red) and RH (blue) zebra events as a function of CML. One bar denotes one event. The lower marker of the bar represents the minimum frequency, the upper marker indicates the highest recorded frequency of the zebra event. Left: Histogram of the frequency distribution of the minimum and maximum frequency values of each LH polarized event. Right: Histogram of the frequency distribution of the minimum and maximum frequency values of each RH polarized event. The box size is 1 MHz.

These histograms contain only the minimum and maximum frequency value of each event, that are also displayed in the figure in the centre. The red and blue distribution differ significantly in the overall range of frequencies and the maxima of the distributions.

When observing a zebra event in a CML interval of 100° to 160° one can thus expect the following properties:

- an event that is most likely RH polarized
- an event that emerges from the northern Jovian hemisphere
- an event with a larger number of individual zebra stripes
- an event that is spread over wider frequency ranges
- an event that arises in ranges with higher frequency values.

These characteristics could possibly be attributed to the Jovian magnetic field. This will be discussed in more detail in section 5.1. On the other hand, events that occur in the LH polarized region (300° to 60° CML) and emerge from the southern hemisphere can be described as events with smaller numbers of individual stripes that are spread over smaller ranges of frequencies and arise in lower frequency ranges. The properties of the two groups of structures (either classified by the CML or by the sense of polarization with frequencies f_R for RH and f_L for LH polarized events) are compared in Figure 27.

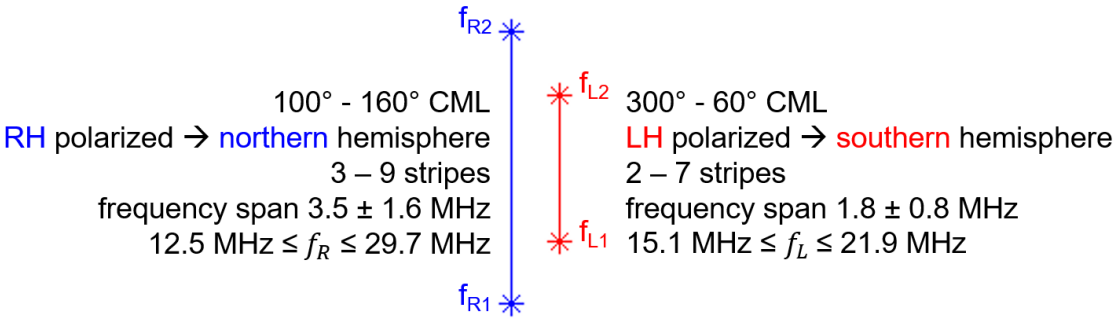

Figure 27: Comparison of zebra structure properties. f_R labels RH, f_L LH polarized events.

5 Discussion

The aim of the statistical analysis of the Jovian zebra spectral structures is to provide the basis to understand the generation mechanism and relate it to already known phenomena. The most important insights obtained from the data analysis in chapter 4 are:

- zebra structures are a non-Io related phenomenon
- within two active regions of CML the appearance of zebra structures is more likely
- the events are highly polarized
- they span from approx. 1 to 10 min duration in time
- they have been registered in frequency ranges between 12.5 and 29.7 MHz
- the individual stripes are separated between 0.2 and 3.7 MHz
- the bandwidth *df* of one stripe ranges between 0.1 and 0.4 MHz with tendencies to values between 0.1 and 0.2 MHz
- the bandwidth *df* is significantly smaller than the frequency spacing Δf: $df \ll \Delta f$

The two regions of active CML have been found to emit either RH or LH polarized radiation:

- 100° to 160° CML: RH polarized
- 300° to 60° CML: LH polarized
- and are separated by approx. 200° in CML (visible as distance between the maxima in the RH and LH distributions).

Subsequently, the sense of polarization defines the hemisphere of origin on Jupiter, as it is known that (see section 2.12)

- RH polarized radiation emerges from the northern hemisphere and
- LH polarized radiation is emitted from the southern hemisphere.

These findings are a first step towards the understanding of the generation of zebra structures. By knowing either the CML or the sense of polarization of the structure one can easily deduce the hemisphere of origin. The events can so be localized.

Differences between RH and LH polarized events can be detected. RH polarized events are observed slightly more often compared to LH polarized events (24 RH/18 LH). As already discussed in section 4.2 this imbalance could possibly be attributed to the D_e-influence. Apart from that, RH polarized events occur in higher frequency ranges, where they stretch across greater frequency intervals with a larger number of stripes (see Figure 27). The Jovian magnetic field is known to be asymmetric with higher field intensities on the northern hemisphere [10]. Therefore an impact of the magnetic field is strongly suggested. This potential influence on the zebra process will be discussed in the following section. The chapter is completed by an approach to the generation mechanism which includes an estimation of the generation site of the zebra structures and the application of the DPR theory.

5.1 Influence of the magnetic field

Several clues on the possible influence of the magnetic field on the zebra spectral structures were found during the data analysis, particularly when considering RH and LH polarized events separately:

- RH polarized events feature a larger number of stripes (3 - 9 stripes) and are spread over a larger frequency interval of 3.5 ± 1.6 MHz on average compared to LH polarized events. These events have 2 - 7 stripes and are spread over a smaller frequency interval of 1.8 ± 0.8 MHz.
- RH polarized events cover a wider overall frequency range (12.5 to 29.7 MHz) with a maximum at higher frequencies than the LH polarized events. LH polarized events can be found between 15.1 and 21.9 MHz.
- The two active regions in CML (corresponding to RH and LH polarized episodes) are approximately 200° apart.

To trace the influence of the magnetic field, the obtained results from the zebra structure analysis have to be compared to the Jovian magnetic field configuration. The two panels on top of Figure 28 show the surface magnetic flux density of the northern and southern hemisphere of Jupiter according to the VIP4-model (see section 2.10). The magnetic field is expressed by the physical value B, the magnetic flux density (for more details see section 2.11).

As can be clearly seen in Figure 28, the strongest flux densities can be found on the northern hemisphere. The highest values ($B > 9$ G with regard to the highest values on the southern hemisphere) on the northern hemisphere appear over almost all latitudes (10° to 80°) and longitudes from 160° to 260°. This large region on the northern hemisphere is comparable to the active CML region where RH polarized zebra events occur (100° to 160° CML). The ranges do not coincide exactly because the CML values retrieved from the observations represent the position of the observer and not the exact position of the source itself. Reconciling these values requires further knowledge of directional patterns which has not been obtained so far. Nevertheless, the correspondence of the active region on the northern hemisphere derived from the analysis of zebra structures and the magnetically active region on Jupiter is evident. There are more aspects fortifying the influence of the magnetic field on the zebra process. RH polarized events are spread over larger frequency intervals, arise in ranges with higher frequencies and feature larger numbers of stripes. These facts can also be attributed to the magnetic field that is significantly stronger in the northern hemisphere. LH polarized zebra events are known to emerge from the southern hemisphere in a CML interval of 300° to 60°. For latitudes -50° to -90° this corresponds to the region with the highest magnetic flux density values on the southern Jovian hemisphere. From other processes driven by the magnetic field on Jupiter, such as auroral emissions, one knows that they take place in high latitudes as well. Therefore the influence of the magnetic field can be undoubtedly claimed for LH polarized zebra events.

Another indication that is linked to the magnetic field configuration on Jupiter is the CML "distance" of maxima of field values on the northern and southern hemisphere and the distance between maximal occurrence of RH and LH polarized events. The maxima of the magnetic field structure on the northern and southern hemisphere are separated by

approx. 200° when counted over 0°. For the zebra events this distance is approximately 200° as well, the maximum for RH polarized events lies around 140° CML, the maximum for LH polarized events around 340°. For illustrating this fact the CML distribution of the zebra episodes from Figure 22 is once more shown in the lower panels of Figure 28.

In summary, the considerations drawn in this section indeed confirm the influence on the location of the radio source of the Jovian magnetic field.

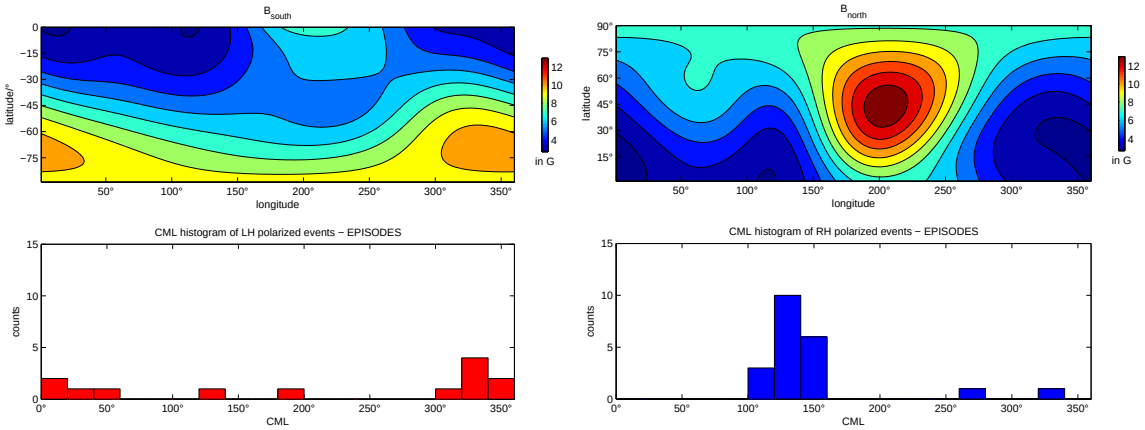

Figure 28: Comparison of the Jovian magnetic field and occurrences of zebra structures with respect to CML. The upper panels show the magnetic flux density for the southern (left, B_{south}) and northern hemisphere (right, B_{north}) separately according to the VIP4-model. The lower panels display the already known CML distributions of LH and RH polarized episodes (Figure 22).

5.2 Double Plasma Resonance as possible generation mechanism of zebra structures

Zebra structures have already been reported at the Sun and Jupiter before. Those effects were observed in higher (GHz) or lower (kHz) frequency ranges. However, both phenomena have been explained by the Double Plasma Resonance (DPR, see section 2.3) theory. It is reasonable to try to attribute the Jovian DAM zebra to the same process. The CMI mechanism that explains planetary radio phenomena in general (see section 2.2) is definitely not able to describe zebra patterns.

First, an estimation of the generation site of the zebra structures will be performed. Thereafter the DPR theory will be used to obtain a specific plasma property, the electron density n_e, to test if the model yields satisfactory results.

5.2.1 Estimation of generation site

Knowing the CML and sense of polarization of a zebra incident enables the localization of generation of the event. The longitude on Jupiter is defined by the recording of the CML value. The corresponding hemisphere is predestined by the sense of polarization. Another property can be estimated by assuming a certain process of generation to be valid for the Jovian zebra structures. As mentioned above, similar phenomena have been observed in lower frequency regions at Jupiter as well as at the Sun. For these cases the DPR turned out to be the favoured theoretical explanation. Therefore, the generation of zebra patterns

should be more likely if the zebra frequency f_z equals an integer multiple s of the electron cyclotron frequency f_{ce} [12]:

$$f_z = s f_{ce}$$

It is then easily possible to obtain an estimation for the lowest possible site of origin above Jupiter's surface of the zebra event. Since the DPR can only be applied when $f_{pe} > f_{ce}$, this corresponds to the harmonic $s = 2$. Then the zebra frequency equals $f_z = 2\ f_{ce}$. With the rule of thumb for the relation between the magnetic flux density B and the cyclotron frequency f_{ce} (valid for electrons),

$$B = f_{ce}/2.8$$

with $[B]$ = G and $[f_{ce}]$ = MHz and the $1/r^3$-dependence (dipole) as a first approximation of the magnetic flux density B on the reference value B_0,

$$B = \frac{B_0}{r^3}$$

the frequency ranges of the zebra events can be converted into distance r_c from Jupiter's centre:

$$r_c = \sqrt[3]{\frac{s\ 2.8 B_{max}}{f_z}}$$

For B_{max} the maximum value of the Jovian magnetic flux density of the corresponding hemisphere is chosen according to the VIP4-model:

- northern hemisphere $B_{max,n} = 13.70$ G
- southern hemisphere $B_{max,s} = 10.54$ G

Those maximum values allow the estimation of the closest distances from Jupiter. The higher the magnetic flux density, the closer to the Jovian surface the emission can be generated. For the northern hemisphere the highest magnetic flux densities occur over almost all latitudes, in the southern hemisphere in latitudes from -50° to -90°.

The results of transferring frequency into distance from Jupiter's centre are displayed for LH and RH polarized events separately in Figure 29. The upper panels (left for LH, right for RH polarized events) show the closest of potential generation site distances as a function of CML (black markers) for each zebra event. The distance r_c from the Jovian centre is given in relation to the Jovian radius R_J. The highest stripe (corresponds to the highest frequency value) of each zebra event is assumed to correspond to $s = 2$. The stripes with lower frequencies correspond to higher harmonics which are generated at greater distances from Jupiter. The lower panel illustrates the frequency range as a function of CML as in Figure 26. A calculated distance value at a certain CML corresponds to the zebra event at the same CML in the frequency range panel.

Comparing the RH and LH polarized events with their closest possible generation sites yields analogous results. Independent of the sense of polarization the events originate at similar distances from Jupiter, predominantly around 0.5 R_J above Jupiter's surface. This connection reveals that the DPR approach might lead to the right direction of understanding the generation mechanism of the zebra phenomenon.

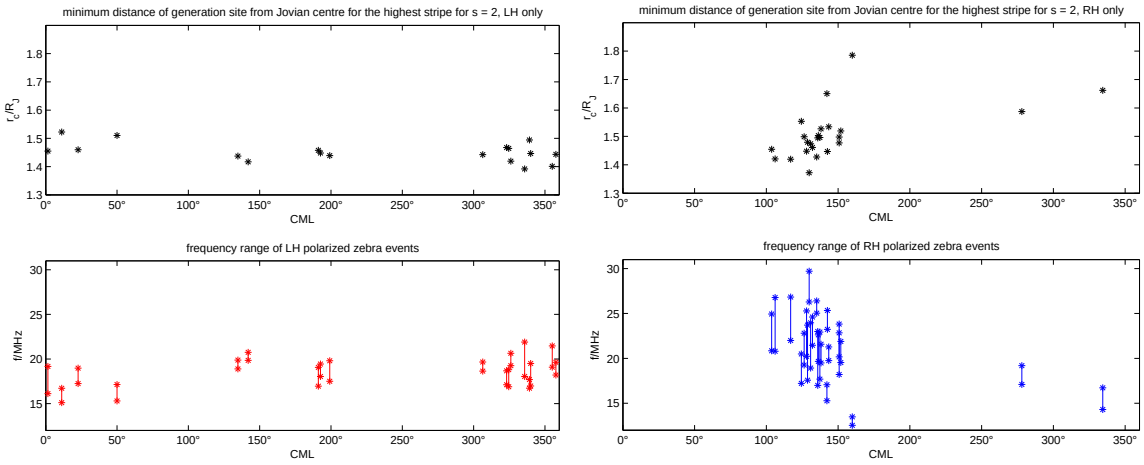

Figure 29: Minimum distance r_c of generation site from Jupiter's centre and frequency range of LH (left) and RH (right) polarized events. The upper panels show the closest of potential generation site distances as a function of CML for each highest stripe of the zebra events (black) for $s = 2$. The distance r_c is given in relation to the Jovian radius R_J. The lower panels illustrate the frequency range (red for LH, blue for RH) as a function of CML as in Figure 26. Distances at a certain CML correspond to the event at the same CML in the frequency range panel.

5.2.2 Applying the DPR theory

The DPR model is exemplarily applied on one Jovian DAM zebra structure to find out whether this theory is capable of explaining the phenomenon.

The zebra event chosen for the application of the DPR occurred on Oct 28, 2013 between 23:46:00 and 23:51:00 UT and can be seen in Figure 18a. The stripes no. 1 to 4 at 23:48:30 UT with frequencies $f_1 \approx 17$ MHz, $f_2 \approx 19$ MHz, $f_3 \approx 20.5$ MHz, $f_4 \approx 22$ MHz are used for the evaluation. The event is RH polarized, thus the corresponding maximum magnetic flux density for the northern hemisphere is $B_{max,n} = 13.70$ G.

As mentioned in section 5.2.1 the generation of zebra stripes is more likely if the zebra frequency f_z equals an integer multiple s of the electron cyclotron frequency f_{ce} [12]:

$$f_z = s f_{ce}$$

With the rule of thumb,

$$f_{ce} = 2.8\ B$$

where $[B] = \mathrm{G}$ and $[f_{ce}] = \mathrm{MHz}$, and the $1/r^3$-dependence (dipole) as a first approximation of the magnetic flux density B on the reference value B_0,

$$B = \frac{B_0}{r^3}$$

it is easy to depict the relation between the zebra frequency f_z, the distance from Jupiter's centre r_c and the harmonic number s:

$$f_z = s\ 2.8\ \frac{B_0}{r_c^3}$$

This relation is illustrated in Figure 30. The x-axis represents the distance above Jupiter's surface r in relation to the Jovian radius R_J, the y-axis shows the zebra frequency f_z. The coloured curves are the profiles for various harmonic numbers s between 2 and 10. The horizontal black lines mark the frequencies of the 4 selected zebra stripes from 17 to 22 MHz. The stripes are assigned to harmonic numbers (indicated by the black markers): the highest stripe with $f_4 = 22$ MHz is assigned to $s = 2$, stripe no. 3 to $s = 3$, no. 2 to $s = 4$ and no. 1 to $s = 5$. The harmonic number cannot be obtained from any measurement or theory. The selected integers exhibit the lower limit in terms of distance to Jupiter. The higher the harmonic number, the farther away from Jupiter the emission is generated. Greater generation distances correspond to lower frequencies. Attaching ascending harmonic numbers to descending zebra stripes is thus appropriate.

Another aspect has to be accounted for when setting up the framework for applying the theory. As the DPR model also gains access to plasma parameters such as the electron density (see below), the physical circumstances have to be considered. The electron density decreases with increasing distance from Jupiter. Therefore, the highest calculated plasma density value is assigned to the closest position from Jupiter, which corresponds to $s = 2$. If the model provides correct predictions, the highest density values have to be found in close vicinity of Jupiter.

In the next step the mentioned electron densities are calculated. By assuming the generation frequency f_z to be equal to the plasma frequency f_p,

$$f_p = \frac{1}{2\pi}\sqrt{\frac{n_e\ e^2}{m_e\ \epsilon_0}}$$

with n_e the electron density, e the elementary electric charge ($e = 1.6 \cdot 10^{-19}$ C), m_e the electron mass ($m_e = 9.1 \cdot 10^{-31}$ kg), and ϵ_0 the electric constant ($\epsilon_0 = 8.9 \cdot 10^{-12}\ \frac{\mathrm{As}}{\mathrm{Vm}}$), the electron density can be derived:

$$n_e = \frac{4\pi^2 f_p^2\ m_e\ \epsilon_0}{e^2}$$

The calculated values in cm^{-3} are displayed in Figure 30 and range from

$$3.6 \cdot 10^6 \leq n_e \leq 6.0 \cdot 10^6\ \mathrm{cm}^{-3}$$

for the selected zebra event. The maximum recorded zebra frequency of 29.7 MHz would correspond to an electron density of $n_e = 1.1 \cdot 10^7\ \mathrm{cm}^{-3}$. Observations by the Voyager spacecraft showed that the density in the Jovian ionosphere is $n_e \lesssim 2 \cdot 10^5\ \mathrm{cm}^{-3}$ at an altitude of $h \approx 2000$ km corresponding to 0.03 R_J. Moreover, the decrease in plasma density in the region 2000 km $\lesssim h \lesssim$ 6000 km ($\approx$ 0.03 - 0.08 R_J) is exponential with the scale height $H \approx 960$ km ($\approx 0.01\ R_J$) [58]. The estimated electron density values for the generation sites of zebra structures exceed those quantities by more than one magnitude and cannot be brought into accordance with the known conditions surrounding Jupiter. Even at a distance of 1.5 R_J the electron density is $n_e = 3.6 \cdot 10^6\ \mathrm{cm}^{-3}$ according to the DPR model in the presented example, which is far too high for this region around Jupiter. In consequence it is strongly suggested that the DPR model for electrons is not the right theory to explain the zebra events.

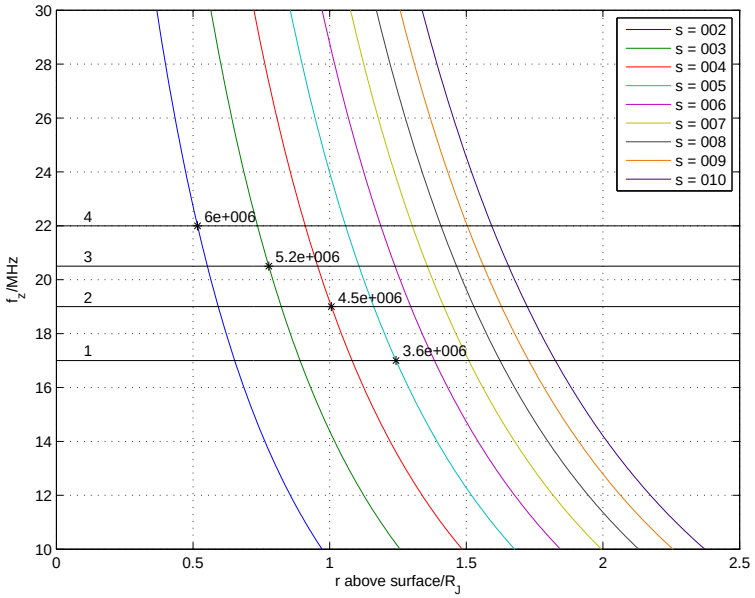

Figure 30: Relation between the zebra frequency f_z, the distance r from Jupiter and the harmonic number s according to the DPR model for one particular part of the event on Oct 28, 2013. The x-axis represents the distance r above Jupiter's surface in relation to the Jovian radius R_J, the y-axis shows the zebra frequency f_z. The coloured curves are the profiles for various harmonic numbers s between 2 and 10. The horizontal black lines mark the frequencies of the 4 selected zebra stripes from 17 to 22 MHz. The stripes are assigned to harmonic numbers (indicated by the black markers): the highest stripe (no. 4) with $f_4 = 22$ MHz to $s = 2$, stripe no. 3 to $s = 3$, no. 2 to $s = 4$, and no. 1 to $s = 5$. The figures next to the black markers represent the calculated electron densities n_e in cm^{-3}.

Apart from the many necessary assumptions to apply the model to the zebra phenomenon, the irrealisable values for the electron density depict a concrete physical value to disprove the feasibility of the DPR model in the presented set-up. Nevertheless, the DPR model does not represent a completely absurd theoretical approach, as it has already been successfully applied to other zebra phenomena at Jupiter and the Sun. Minor modifications of the approved theory may lead to the breakthrough of describing the Jovian DAM zebra structures. A first step in that direction could be the implementation of the DPR theory at ion cyclotron harmonics which requires a more complicated approach [59] combined with additional observations and theoretical investigations. This would mark a proposition that has not been studied so far where a promising outcome could be imagined.

6 Conclusion

Zebra spectral structures in the Jovian DAM emissions have been registered for the first time during two observation campaigns from September 2012 to March 2014 by the URAN-2 telescope. These patterns have not been mentioned in literature so far therefore the detailed characterization of this phenomenon was pursued in this thesis. The investigation of the zebra events revealed that yet another non-Io related radio phenomenon at Jupiter occurs, that can be added to the catalogue of non-Io Jovian radio emissions. In contrast to the studies on zebra patterns in the Jovian kilometric radiation (KOM) [12] in which the patterns could not be localized in respect of Jupiter, the measurements used in this thesis are able to pinpoint the zebra spectral structures. Two zebra-active regions of CML exist on Jupiter. Taking the polarization of the events into consideration, the two regions of CML produce radiation that can be observed as either RH or LH polarized. As the sense of polarization defines the hemisphere where the radiation is generated, the zebra incidents can easily be located in the Jovian coordinate system. By recording the frequency properties the patterns can be described in detail as it has been done for other Jovian radio emissions. Thereby it is clearly possible to identify the structures in the dynamic spectra. As the zebra stripes appear in the frequency range from 12 to 30 MHz they can be precisely observed by URAN-2, which is able to record radiation between 8 and 32 MHz in high frequency and time resolution.

Zebra spectral structures show characteristics that are comparable to solar and Jovian KOM zebra patterns, such as the increase of the frequency spacing between individual stripes with increasing frequency of occurrence. The central result of the statistical analysis of the zebra events - being able to localize the structures in respect of Jupiter - gives rise to explaining the generation process of the phenomenon. Additionally, the frequency properties of the events in the two hemispheres differ significantly. The Jovian attribute that strongly diverges hemispherically is the magnetic field configuration. The northern magnetic field is fairly stronger than the field in the south. Moreover, the maxima of the field in the north and south are separated by approximately the same distance as the maxima of occurrence of zebra events in the two hemispheres. The driving force of the phenomenon has thus been found in accordance to other planetary radio effects. In addition, the influence of the magnetic field enables the restriction on the generation sites in terms of latitude. This coordinate is not accessible by observation by the radio telescope. By assuming the generation sites to be in the areas of strongest magnetic field flux the events can be localized even more exactly.

The Double Plasma Resonance theory of electrons is widely accepted as the theoretical background for the solar and Jovian KOM zebra patterns and also relies on the magnetic field as trigger of the emission. By applying this theory an estimation for the lowest possible altitude of the generation site can be obtained. Hence, the anticipated plasma environment of the generation site can be determined. However, the applicability of the theory for the Jovian DAM zebra spectral structures failed as the calculation of one particular plasma parameter, the electron density, predicts values incommensurate with the conditions in the Jovian surroundings. Yet, this is not seen as a setback as the DPR has already been approved for similar processes. Likely, a slight alteration of the applied assumptions has to be performed to eventually describe the Jovian DAM zebra phenomenon theoretically.

Nonetheless this thesis led to notable progress in the field of describing the zebra spectral structures in Jovian DAM. The structures can now be recognized more easily as their properties are well-defined and recorded. The events can be localized even more precisely by taking the magnetic field into account, that once more turned out to be the driving force of a planetary radio phenomenon. The test of the accepted DPR theory under certain conditions forms an important contribution to the complete understanding of the investigated process.

7 Outlook

When dealing with a novel phenomenon within the framework of a master thesis the topic can by no means be covered completely. Several aspects have to be left open, which should be addressed here.

Currently, a rather small amount of events was used for investigation. In order to substantiate the statistical results more data needs to be inspected. A lot more observations from URAN-2 are available that just have to be scanned for additional zebra patterns. Within the scope of retrieving more data, the cumbersome data acquisition process could be facilitated by the following improvements. Selecting potential zebra events from the dynamic spectra was performed visually. The statistical analysis provides plenty of data that could now be used for image recognition. The vast amount of observations from URAN-2 could so be easily browsed for more zebra structures. Also the data from the individual events was retrieved manually. Expanding the Spectra Viewer tool to be able to identify the stripes automatically by virtue of their high intensities above the background and storing the obtained frequency properties and the characteristics of each event (date, time, CML, Io phase etc.) would gain access to a lot more information on the phenomenon.

The technical capabilities of URAN-2 are not fully exploited by now. The calibration process to obtain reliable measurements of the full polarization state of the incident radiation has still to be completed. This additional information could give more details on the emission process, the wave propagation and the plasma the radiation propagated.

Not only URAN-2 observes Jovian radio emissions. UTR-2 (Kharkiv, Ukraine) and NDA (Nançay, France) record this radiation as well. Simultaneous measurements could thus be compared to verify the results from URAN-2. Also local influences and ionospheric scintillations could be estimated in comparative studies.

In order to describe the Jovian DAM zebra patterns theoretically, the DPR for electrons proved to be inapplicable. Applying said theory on ions would be a first step towards a solution of this dilemma and would form a totally new approach to the phenomenon that could be presented to the scientific community.

At this point it should be noted, that the results of the present study are going to be published in near future in the journal *Astronomy & Astrophysics*.

8 Summary

Newly observed spectral structures in the Jovian DAM have been investigated in this thesis. These zebra-stripe like patterns occur in a frequency range between ca. 12 and 30 MHz. Dynamic spectra recorded at the URAN-2 radio telescope in Poltava, Ukraine, have been scanned for structures that consist of individual quasi-parallel stripes. 42 events could be retrieved and have been characterized by several parameters recorded by the telescope (see chapter 3). The central result of the subsequent statistical analysis (see chapter 4) can be seen in Figure 31. It shows the distribution of the zebra events in CML and frequency as well as their sense of polarization (blue for RH, red for LH). One bar denotes one event. The lower marker of the bar marks the minimum frequency, the upper marker the maximum frequency of said event.

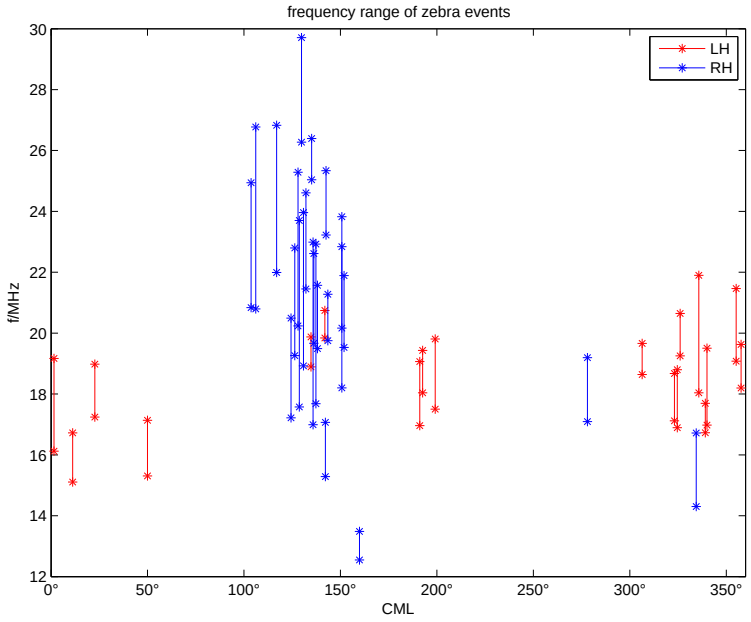

Figure 31: Central result of the statistical analysis of zebra events. The frequency range of LH (red) and RH (blue) zebra events is displayed as a function of CML. One bar denotes one event. The lower marker of the bar represents the minimum frequency, the upper marker indicates the highest recorded frequency of the zebra event.

A lot of information about the zebra structures can be retrieved from this illustration:

- Two active regions of CML can be identified, from 100° to 160° and from 300° to 60° (counted over 0°).
- These two regions emit either RH (blue) or LH (red) polarized radiation.
- Due to an observational effect described in section 2.12 the RH polarized events can be assigned to the northern Jovian hemisphere, LH polarized events are generated in the southern hemisphere.
- The two regions are separated by approx. 200°. This is in accordance with the distance between the areas of maximum magnetic field intensity on the Jovian hemispheres.

The zebra structures can therefore be localized in respect of Jupiter. Moreover, zebra structures are a non-Io related phenomenon, as no influence of the Io phase could be detected. The events last between 1 and 10 min in time. Several frequency properties could be obtained. A selection of certain properties is once more summarized in Figure 32.

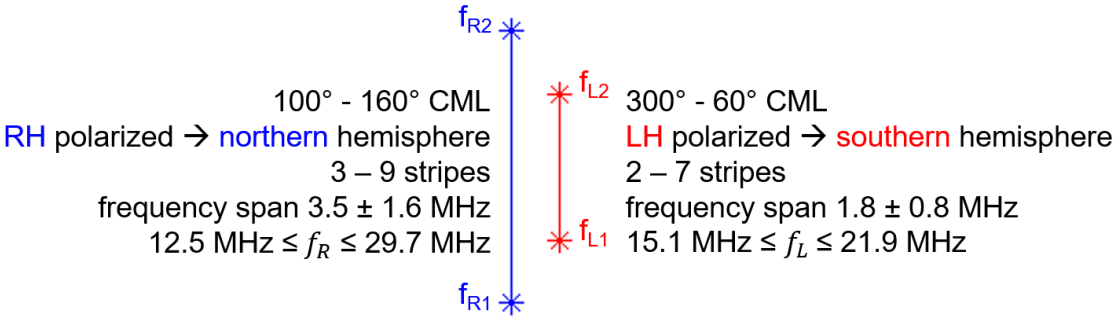

Figure 32: Comparison of zebra structure properties. f_R labels RH, f_L LH polarized events.

On the basis of these results the influence of the magnetic field was confirmed. By applying the Double Plasma Resonance theory for electrons, which is widely accepted for the explanation of solar and Jovian KOM zebra patterns, an estimation of the closest possible site of generation was obtained. However, when calculating a concrete plasma parameter, the electron density, the theory provides inappropriate values that cannot be realized in the environment of Jupiter. Further investigations are therefore indispensable.

List of Abbreviations

CME	coronal mass ejections
CMI	Cyclotron Maser Instability
CML	Central Meridian Longitude
DAM	decametric radio emission
DPR	Double Plasma Resonance
GURT	Giant Ukrainian Radio Telescope
IAU	International Astronomical Union
IEEE	Institute of Electrical and Electronics Engineers
KOM	kilometric radio emission
LH	left-hand
LOFAR	Low Frequency Array
LOIS	LOFAR Outrigger in Scandinavia
LWA	Low Wavelength Array
NASA	National Aeronautics and Space Administration
NASU	National Academy of Sciences of Ukraine
NDA	Nançay Decametric Array
NenuFAR	New Extension in Nançay Upgrading LOFAR
RH	right-hand
SCET	spacecraft event time
SED	Saturn electric discharges
SIRA	Solar Imaging Radio Array
SKA	Square Kilometre Array
STEREO	Solar Terrestrial Relations Observatory
URAN	Ukrainian Radio Interferometer of NASU
UTR-2	Ukrainian T-shaped radio telescope, second modification
VLBI	Very Long Baseline Interferometry

List of Figures

List of Tables

References

[1] B. F. Burke and K. L. Franklin. Observations of a variable radio source associated with the planet Jupiter. *J. Geophys. Res.*, 60(2):213–217, 1955.

[2] P. Zarka. Auroral radio emissions at the outer planets: Observations and theories. *Journal of Geophysical Research*, 103(9):20159–20194, 1998.

[3] P. Zarka. Radio and plasma waves at the outer planets. *Advances in Space Research*, 33(11):2045–2060, 2004.

[4] P. Zarka and W. S. Kurth. Radio wave emission from the outer planets before Cassini. *Space Science Reviews*, 116(1-2):371–397, 2005.

[5] P. Zarka, J. Queinnec, B. P. Ryabov, V. B. Ryabov, V. A. Shevchenka, A. V. Arkhipov, H. O. Rucker, L. Denis, A. Gerbault, P. Dierich, and C. Rosolen. Ground-Based High Sensitivity Radio Astronomy at Decameter Wavelengths. In H. O. Rucker, S. J. Bauer, and A. Lecacheux, editors, *Planetary Radio Emissions IV*, page 101. Austrian Academy of Sciences Press, Vienna, 1997.

[6] F. Genova. Extended Ground Based Observations of Jupiter's Decametric Radiation. In H. O. Rucker, S. J. Bauer, and B. M. Pedersen, editors, *Planetary Radio Emissions II*, pages 53–68. Austrian Academy of Sciences Press, Vienna, 1987.

[7] A. A. Konovalenko, A. Lecacheux, C. Rosolen, and H. O. Rucker. New Instrumentations and methods for the low frequency planetary radio astronomy. In H. O. Rucker, M. L. Kaiser, and Y. Leblanc, editors, *Planetary Radio Emissions V*, pages 1–15. Austrian Academy of Sciences Press, Vienna, 1996.

[8] E. F. Milone and W. J. F. Wilson. *Solar System Astrophysics: Planetary Atmospheres and the Outer Solar System*. Springer, 2nd edition, 2014.

[9] C. S. Wu. Cyclotron Maser Instability and its applications. In H. O. Rucker, S. J. Bauer, and B. M. Pedersen, editors, *Planetary Radio Emission II*, pages 387–394. Austrian Academy of Sciences Press, Vienna, 1988.

[10] H. O. Rucker. Planetenmagnetosphären. In *Erde und Planeten - Band 7. Lehrbuch der Experimentalphysik*, pages 527–604. Walter de Gruyter, Berlin, New York, 2nd edition, 2001.

[11] V. V. Zheleznyakov and E. Y. Zlotnik. Cyclotron wave instability in the corona and origin of solar radio emission with fine structure. III. Origin of Zebra-Pattern. *Solar Physics*, 44:461–470, 1975.

[12] A. A. Kuznetsov and V. G. Vlasov. Formation of zebra pattern in low-frequency Jovian radio emission. *Planetary and Space Science*, 75(1):167–172, 2013.

[13] B. Alder. Dynamic spectra. In *Radio Astronomy*, Methods in computational physics, pages 44, 197. Elsevier Science, Amsterdam, 1975.

[14] G.A. Reider. Magnetooptischer Effekt. In *Photonik. Ein Einführung in die Grundlagen*, pages 81–82. SpringerWienNewYork, Wien, 2nd edition, 2005.

[15] D. Meschede. Faraday-Rotatoren. In *Optik, Licht und Laser*, page 146. Vieweg+Teubner, Wiesbaden, 3rd edition, 2008.

[16] F.F. Chen. *Introduction to Plasma Physics and Controlled Fusion.* Plenum Press, New York, 2nd edition, 1984.

[17] H. Bradt. Faraday rotation. In *Astrophysics Processes: The Physics of Astronomical Phenomena*, pages 429–430. Cambridge University Press, Cambridge, 1st edition, 2008.

[18] J. A. Phillips, T. C. Ferree, and J. Wang. Earth-based observations of Faraday rotation in radio bursts from Jupiter. *Journal of Geophysical Research,*, 94:5457–5466, 1989.

[19] M. Panchenko, S. Rošker, H. O. Rucker, A. Brazhenko, A. A. Konovalenko, G. Lytvinenko, and P. Zarka. Zebra pattern in decametric radio emission of Jupiter. To be published. *Astronomy & Astrophysics*, 2016.

[20] M. Y. Boudjada, G. A. Dulk, and A. Lecacheux. Faraday Rotation of Jupiter's Decametric Radiation. In H. O. Rucker, S. J. Bauer, and M. L. Kaiser, editors, *Planetary Radio Emissions III*, pages 155–170. Austrian Academy of Sciences Press, Vienna, 1992.

[21] NASA. Atmospheric electromagnetic transmittance or opacity. `https://commons.wikimedia.org/wiki/File:Atmospheric_electromagnetic_opacity.svg`. Accessed: Nov 24, 2015.

[22] E. K. Bigg. Influence of the Satellite Io on Jupiter's Decametric Emission. *Nature*, 203(4949):1008–1010, 1964.

[23] T. D. Carr, M. D. Desch, and J. K. Alexander. Figure - Io related and non-Io related sources. In A. J. Dessler, editor, *Physics of the Jovian Magnetosphere*, chapter Phenomenology of magnetospheric radio emissions, page 259. Cambridge University Press, Cambridge, 1983.

[24] L. Pan and P. Yin. Analysis of Polar Ionospheric Scintillation Characteristics Based on GPS Data. In J. Sun, W. Jiao, H. Wu, and M. Lu, editors, *China Satellite Navigation Conference (CSNC) 2014 Proceedings: Volume I*, pages 11–18. Springer-Verlag, Berlin Heidelberg, 2014.

[25] J. Aarons. Global Morphology of Ionospheric Scintillations. *Proceedings of the IEEE*, 70(4):360–378, 1982.

[26] N. F. Ness. Planetary Magnetic Fields: Salient Characteristics. In H. O. Rucker, S. J. Bauer, and M. L. Kaiser, editors, *Planetary Radio Emissions III*, pages 1–12. Austrian Academy of Sciences Press, Vienna, 1992.

[27] S. Miller, N. Achilleos, G. E. Ballester, T. R. Geballe, R. D. Joseph, R. Prange, D. Rego, T. S. Stallard, J. Tennyson, L. M. Trafton, and J. H. Waite. The role of H3+ in planetary atmospheres. *Philosophical Transactions of the Royal Society A*, 358(1774):2485–2502, 2000.

[28] Max Planck Institute for Solar System Research. Jovian magnetosphere. `https://www2.mps.mpg.de/en/aktuelles/pressenotizen/pressenotiz_20081210.html`. Accessed: Jan 11, 2016.

[29] M. H. Acuna and N. F. Ness. The main magnetic field of Jupiter. *Journal of Geophysical Research*, 81(16):2917–2922, 1976.

[30] N. F. Ness. The Magnetic Environment of the known Radio Planets. In H. O. Rucker, S. J. Bauer, and B. M. Pedersen, editors, *Planetary Radio Emissions II*. Austrian Academy of Sciences Press, Vienna, 1988.

[31] J. E. P. Connerney, M. H. Acuña, N. F. Ness, and T. Satoh. New models of Jupiter's magnetic field constrained by the Io flux tube footprint. *Journal of Geophysical Research*, 103(A6):11929, 1998.

[32] S. L. G. Hess, B. Bonfond, P. Zarka, and D. Grodent. Model of the Jovian magnetic field topology constrained by the Io auroral emissions. *Journal of Geophysical Research: Space Physics*, 116(5):1–19, 2011.

[33] E. J. Rothwell and M. J. Cloud. *Electromagnetics*. Electrical Engineering Textbook Series. Taylor & Francis, 2010.

[34] D. Meschede. Polarisation des Lichts. In *Gerthsen Physik*, page 541. Springer-Verlag, Berlin, Heidelberg, 22nd edition, 2004.

[35] Polarisation (Linear), Polarisation (Circular), Polarisation (Elliptical). `https://commons.wikimedia.org/wiki/File:Polarisation_%28Elliptical%29.svg`. Accessed: Jan 07, 2016.

[36] IAU General Assembly Meeting, Commission 40 (Radio Astronomy, Radioastronomie), 1973.

[37] IEEE Committee Antenna Standard 149-1979 (R2008). IEEE Standard Test Procedures for Antennas, 1979.

[38] R. Feynman, R. B. Leighton, and M. Sands. The Feynman Lectures on Physics, Volume I, mainly mechanics, radiation, and heat, Chapter 33-1. `http://www.feynmanlectures.caltech.edu/`. Accessed: Jan 22, 2016.

[39] K. K. Khurana, M. G. Kivelson, V. M. Vasyliunas, N. Krupp, J. Woch, A. Lagg, B. H. Mauk, and W. S. Kurth. The Configuration of Jupiter's Magnetosphere (Chapter 24). In F. Bagenal, T. Dowling, and W. McKinnon, editors, *Jupiter: The Planet, Satellites and Magnetosphere*, pages 593–616. Cambridge University Press, Cambridge, 2004.

[40] A. Lecacheux, G. A. Dulk, and M. Y. Boudjada. The Elliptical Polarization of the Jovian Decametric Emission and the Magnetosphere of Jupiter. In H. O. Rucker, S. J. Bauer, and M. L. Kaiser, editors, *Planetary Radio Emissions III*, pages 147–154. Austrian Academy of Sciences Press, Vienna, 1992.

[41] IRE (1942). Standards on polarization concepts and terminology. Proceedings of the Institute of Radio Engineers 30, no. 7, part III, suppl. IW47.

[42] M. Gargaud. *R - Encyclopedia of Astrobiology.* Springer Berlin Heidelberg, 2011.

[43] G. Verschuur. *The Invisible Universe. The Story of Radio Astronomy.* Springer, 3rd edition, 2015.

[44] French NenuFAR telescope granted SKA Pathfinder status. `https://www.skatelescope.org/news/french-nenufar-telescope-granted-ska-pathfinder-status/`. Accessed: Jan 26, 2016.

[45] The project timeline. `https://www.skatelescope.org/projecttimeline/`. Accessed: Jan 26, 2016.

[46] A. A. Konovalenko, L. Sodin, V. Zakharenko, P. Zarka, O. Ulyanov, M. Sidorchuk, S. Stepkin, P. Tokarsky, V. Melnik, N. Kalinichenko, A. Stanislavsky, V. Koliadin, V. Shepelev, V. Dorovskyy, and A. Koval. The modern radio astronomy network in Ukraine: UTR-2, URAN and GURT. 2015.

[47] A. Lecacheux. A Useful Step Towards Giant New Generation Radio Telescopes for Long Wavelength Radio Astronomy, Radio Astronomy at Long Wavelengths. *Geophysical Monograph*, 119:321–328, 2000.

[48] European Space Agency (ESA). Herschel Observer's Manuel V5.0.3, March 7, 2014. `http://herschel.esac.esa.int/Docs/Herschel/html/ch04s03.html`. Accessed: Jan 27, 2016.

[49] A. A. Konovalenko, H. O. Rucker, A. Lecacheux, V. N. Melnik, I. S. Falkovich, N. N. Kalinichenko, M. R. Olyak, and A. V. Megn. Utilizing existing decameter radio telescopes as pathfinders towards LOFAR - LWA - LOIS science and technology. In H. O. Rucker, W. S. Kurth, and G. Mann, editors, *Planetary Radio Emissions VI*, pages 507–518. Austrian Academy of Sciences Press, Vienna, 2006.

[50] A.V. Megn, S. Ya. Braude, S. L. Rashkovsky, N. K. Sharykin, V. A. Shepelev, G. A. Inyutin, A. D. Khristenko, V. G. Bulatsen, A. I. Brazhenko, V. V. Koshevoj, Yu. V. Romanchev, V. P. Tsesevich, and V. V. Galanin. Decameter wavelength radio interferometer system URAN. *Radiophysics and Radioastronomy*, 2:385–401, 1997.

[51] A. I. Brazhenko, V. G. Bulatsen, R. V. Vashchishin, A. V. Frantsuzenko, A. A. Konovalenko, I. S. Falkovich, E. P. Abranin, O. M. Ulyanov, V. V. Zakharenko, A. Lecacheux, and H. O. Rucker. New decameter radiopolarimeter URAN-2. *Kinematika I Fizika Nebesnykh Tel Suppl.*, 5(43):43–46, 2005.

[52] National Academy of Sciences of Ukraine. URAN-2. `http://rian.kharkov.ua/index.php/ru/decameter-structure/uran-2`. Accessed: Dec 01, 2015.

[53] Ø. Elgaroy. Observations of the Fine Structure of Enhanced Solar Radio Radiation with a Narrow-Band Spectrum Analyser. *Nature*, 184(4690):887–888, 1959.

[54] A. A. Kuznetsov and Yu. T. Tsap. Loss-cone instability and formation of zebra patterns in type IV solar radio bursts. *Solar Physics*, 241(1):127–143, 2007.

[55] G. P. Chernov. Solar radio bursts with drifting stripes in emission and absorption. *Space Science Reviews*, 127(1-4):195–326, 2006.

[56] Ø. Elgaroy. High-Resolution Spectrometry of Enhanced Solar Radio Emission. *Astrophysica Norvegica*, 7(123), 1961.

[57] M. Y. Boudjada, P. H. M. Galopeau, and H. O. Rucker. Study of the modelled occurrence variability of the Jovian decametric emissions. In H. O. Rucker, W. S. Kurth, and G. Mann, editors, *Planetary Radio Emissions VI*, pages 169–174. Austrian Academy of Sciences Press, Vienna, 2006.

[58] D. B. Melrose and G. A. Dulk. On the elliptical polarization of Jupiter's decametric radio emission. *Astronomy & Astrophysics*, 249:250–257, 1991.

[59] E. Y. Zlotnik, V. E. Shaposhnikov, and V. V. Zaitsev. On the origin of zebra pattern in kilometer radiation from Jupiter. In *Proceedings of the All-Russian Annual Conference on Solar Physics (Sept. 25 - 27, 2013)*, St. Petersburg, 2013.

[60] NASA. Jupiter fact sheet. `http://nssdc.gsfc.nasa.gov/planetary/factsheet/jupiterfact.html`. Accessed: Jan 29, 2016.

[61] Zebra. `http://www.foileshop.de/wandtattoo/Tierwelt/Zebra.html`. Accessed: Feb 05, 2016.

Appendix

NASA Jupiter fact sheet [60]

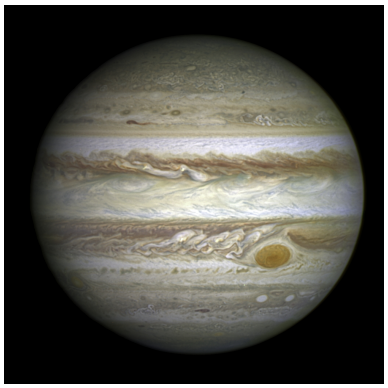

Table 7: Jupiter/Earth Comparison - Bulk parameters

	Jupiter ♃	Earth ♁	Ratio (♃/♁)
Mass (10^{24} kg)	1898.3	6.0	317.8
Volume (10^{10} km^3)	143128	108	1321
Radius (1 bar level) (km)			
Equatorial	71492	6378	11
Polar	66854	6357	11
Volumetric mean radius (km)	69911	6371	11
Ellipticity	0.06487	0.00335	19.4
Mean density (kg/m^3)	1326	5514	0.2
Gravity (eq., 1 bar) (m/s^2)	24.79	9.80	2.5
Acceleration (eq., 1 bar) (m/s^2)	23.12	9.78	2.4
Escape velocity (km/s)	59.5	11.2	5.3
Bond albedo	0.343	0.306	1.1
Visual magnitude V(1,0)	-9.40	-3.86	-
Solar irradiance (W/m^2)	50.5	1367.6	0.04
Black-body temperature (K)	110.0	254.3	0.43
Moment of inertia (I/MR^2)	0.254	0.331	0.77
Number of natural satellites	67	1	67
Planetary ring system	Yes	No	-

Table 8: Jupiter/Earth Comparison - Orbital parameters

	Jupiter ♃	Earth ♁	Ratio (♃/♁)
Semimajor axis (10^6 km)	778.57	149.60	5.20
Sidereal orbit period (days)	4332.589	365.256	11.86
Tropical orbit period (days)	4330.595	365.242	11.86
Perihelion (10^6 km)	740.52	147.09	5.03
Aphelion (10^6 km)	816.62	152.10	5.37
Synodic period (days)	398.88	-	-
Mean orbital velocity (km/s)	13.06	29.78	0.44
Max. orbital velocity (km/s)	13.72	30.29	0.45
Min. orbital velocity (km/s)	12.44	29.29	0.43
Orbit inclination (deg)	1.304	0.000	-
Orbit eccentricity	0.0489	0.0167	2.93
Sidereal rotation period (hours)	9.9250	23.9345	0.42
Length of day (hrs)	9.9259	24.0000	0.41
Inclination of equator (deg)	3.13	23.44	0.13

Table 9: Jupiter observational parameters

Distance from Earth	
Minimum (10^6 km)	588.5
Maximum (10^6 km)	968.1
Apparent diameter from Earth	
Minimum (seconds of arc)	50.1
Maximum (seconds of arc)	29.8
Mean values at opposition from Earth	
Distance from Earth (10^6 km)	628.8
Apparent diameter (seconds of arc)	46.9
Apparent visual magnitude	-2.7
Maximum apparent visual magnitude	-2.9

Table 10: Jovian Magnetosphere

Dipole field strength (G/R_J^3)	4.28
Dipole tilt to rotational axis (deg)	9.6
Longitude of tilt (deg)	201.7
Dipole offset (planet center to dipole center) distance	0.131 R_J
Latitude/Longitude of offset vector (deg)	-8.0/148.6

Goddard Space Flight Center O4 Model
Note: all latitudes/longitudes are given in Jovian System III (1965.0) coordinates.
R_J denotes Jovian radius (71398 km)

Table 11: Jovian Atmosphere

Surface pressure (bar)	$\gg 1000$
Temperature at 1 bar (K/°C)	65/-108
Temperature at 0.1 bar (K/°C)	112/-161
Density at 1 bar (kg/m^3)	0.16
Scale height (km)	27

Table 12: Jupiter's atmospheric composition by volume, uncertainty in parentheses

Major	Molecular hydrogen (H_2) - 89.8% (2.0%)
	Helium (He) - 10.2% (2.0%)
Minor (ppm)	Methane (CH_4) - 3000 (1000)
	Ammonia (NH_3) - 260 (40)
	Hydrogen Deuteride (HD) - 28 (10)
	Ethane (C_2H_6) - 5.8 (1.5)
	Water (H_2O) - 4 (varies with pressure)
Aerosols	Ammonia ice
	Water ice
	Ammonia hydrosulfide

Zebra pictogram from [61]